

Article

Contrasting Modes of Carbonate Precipitation in a Hypersaline Microbial Mat and Their Influence on Biomarker Preservation (Kiritimati, Central Pacific)

Yan Shen ^{1,2,*} , Pablo Suarez-Gonzalez ³  and Joachim Reitner ^{4,5} ¹ SKL Lunar and Planetary Sciences, Macau University of Science and Technology, Taipa, Macau 999078, China² CNSA Macau Center for Space Exploration and Science, Taipa, Macau 999078, China³ Department of Geodynamics, Stratigraphy and Paleontology, Complutense University of Madrid, 28040 Madrid, Spain; pablosuarez@ucm.es⁴ Department of Geobiology, Geoscience Centre, Georg-August-Universität Göttingen, 37077 Göttingen, Germany; jreitne@gwdg.de⁵ 'Origin of Life' Group, Göttingen Academy of Sciences and Humanities, 37073 Göttingen, Germany

* Correspondence: yanshen@must.edu.mo



Citation: Shen, Y.; Suarez-Gonzalez, P.; Reitner, J. Contrasting Modes of Carbonate Precipitation in a Hypersaline Microbial Mat and Their Influence on Biomarker Preservation (Kiritimati, Central Pacific). *Minerals* **2022**, *12*, 267. <https://doi.org/10.3390/min12020267>

Academic Editors: Vincent V. Barbin and Frédéric Marin

Received: 8 January 2022

Accepted: 8 February 2022

Published: 20 February 2022

Publisher's Note: MDPI stays neutral with regard to jurisdictional claims in published maps and institutional affiliations.



Copyright: © 2022 by the authors. Licensee MDPI, Basel, Switzerland. This article is an open access article distributed under the terms and conditions of the Creative Commons Attribution (CC BY) license (<https://creativecommons.org/licenses/by/4.0/>).

Abstract: Microbial mats represented the earliest complex ecosystems on Earth, since fossil mineralized examples (i.e., microbialites) date back to the Archean Eon. Some microbialites contain putative remains of organic matter (OM), however the processes and pathways that lead to the preservation of OM within microbialite minerals are still poorly understood. Here, a multidisciplinary study is presented (including petrographic, mineralogical and organic geochemical analyses), focusing on a modern calcifying mat from a hypersaline lake in the Kiritimati atoll (Central Pacific). The results show that this mat has a complex history, with two main growth phases under hypersaline conditions, separated by an interruption caused by desiccation and/or freshening of the lake. The mineral precipitates of the mat are predominantly aragonitic and two contrasting precipitation modes are observed: the main growth phases of the mat were characterized by the slow formation of irregular micritic particles with micropeloidal textures and subspherical particles, linked to the degradation of the exopolymer (EPS) matrix of the mat; whereas the interruption period was characterized by the rapid development of a thin but laterally continuous crust composed of superposed fibrous aragonite botryoids that entombed their contemporaneous benthic microbial community. These two precipitation modes triggered different preservation pathways for the OM of the mat as the thin crust shows a particular lipid biomarker signature, different from that of other layers and the relatively rapid precipitation of the crust protecting the underlying lipids from degradation, causing them to show a preservation equivalent to that of a modern active microbial community, despite them being >1100 years old. Equivalent thin mineral crusts occur in other microbialite examples and, thus, this study highlights them as excellent targets for the search of well-preserved biomarker signatures in fossil microbialites. Nevertheless, the results of this work warn for extreme caution when interpreting complex microbialite biomarker signatures, advising combined petrographic, mineralogical and geochemical investigations for the different microbialite layers and mineral microfabrics.

Keywords: microbialites; biomarkers; organic matter taphonomy; aragonite; organomineralization; biomineralization; microbial fossils

1. Introduction

Microbial mats (benthic, laminated, mm- to cm-thick microbial communities) probably represented the earliest complex ecosystems on Earth and they are still ubiquitous nowadays, thriving in many different contexts, from freshwater to hypersaline settings, including hot springs and other extreme environments [1–7]. Microbial mats consist of several specialized biotic consortia, and each layer contains different microorganisms

with distinct metabolic activities [8,9]. The fossilized counterparts of microbial mats are microbialites [10], which have an extremely long geological record of ~3.5 Ga [11,12]. Microbialites are most commonly composed of carbonate minerals (with participation of other minerals, such as phosphates, sulphates, silicates, iron minerals and oxides) and putative remains of the organic matter (OM) of their original microbial mats have also been found within some of them [13–15]. Nevertheless, the interpretation of biomarkers and signatures of OM within microbialites is always challenging, given the wide variety of biotic and abiotic factors involved in their complex history, ranging from the paleoenvironment and origin of the OM to its taphonomy and final fossilization [16–21]. In addition, many different organic and inorganic processes can contribute to carbonate precipitation in microbial mats (see reviews in [22,23]), which further complicates the preservation pathways of OM within microbialites and the interpretation of their organic geochemical signatures.

In this work, a modern and actively mineralizing microbial mat is studied, from a hypersaline lake in Kiritimati Island (Central Pacific), the largest atoll in the world. This detailed geomicrobiological study encompasses different petrographic techniques for both organic and mineral components of the microbial mat, as well as mineralogical and organic geochemical analyses, to unravel the complex history of the mat. This allows one to interpret the different ways in which carbonate precipitated within the mat and to understand how precipitation modes controlled the different biomarker signatures observed, providing an excellent example of the integration of organic geochemical, petrographic and mineralogical analyses, and indicating that these techniques should be always coupled to elucidate the origin and taphonomy of OM within microbialites.

2. Materials and Methods

2.1. Site Description and Sample Collection

Kiritimati (formerly Christmas Island) is the world's largest atoll, with a surface area c. 360 km². It is located in the central Pacific and close to the Equator (1°55' N, 157°25' W). The island harbors approximately 500 lakes with salinities ranging from brackish to hypersaline [24,25], in many of which, well-developed microbial mats occur [26,27]. These microbial mats are often developed on top of subfossil reef-structures and microbialites that represent older and almost fully mineralized generations of microbial mats [5,27,28].

In general, Kiritimati has an arid climate and is mostly controlled by the El Niño–Southern Oscillation (ENSO). Recharge of lakes occurs as a result of heavy rains during El Niño wet events, leading to a decrease in lake salinities. During La Niña dry events, reduced precipitation and higher evaporation induce an increase in lake salinities [24,25,29].

Sampling was carried out during an expedition to Kiritimati in March 2011, with the required research permit issued by the Environment and Conservation Division of the Ministry of Environment, Lands and Agriculture Developments (MELAD) of the Republic of Kiribati. The microbial mat studied in this work is 10 cm thick and it was collected from the center of Lake 2 (Figure 1; 01°50'49.35" N, 157°21'36.32" W) at water depth c. 4 m [30]. The salinity of Lake 2 was 97‰ in 2002 and 125‰ in 2011 (unpublished own data). Blumenberg et al. [30] analyzed some aspects of the same mat studied here, and divided it in five layers. Nevertheless, given the more comprehensive and detailed analysis conducted here, a different layer division has been made (see Section 3 Results, below).

In order to compare the mineralization of the studied modern mat with that of older counterparts, we also conducted petrographic studies of thin sections of subfossil microbialites from another lake on Kiritimati, sampled in the same campaign (Lake 21 01°57'45.63" N, 157°19'53.03" W). The studied subfossil microbialite from Lake 21 occurs immediately below the modern active microbial mat at the bottom of the lake [28].

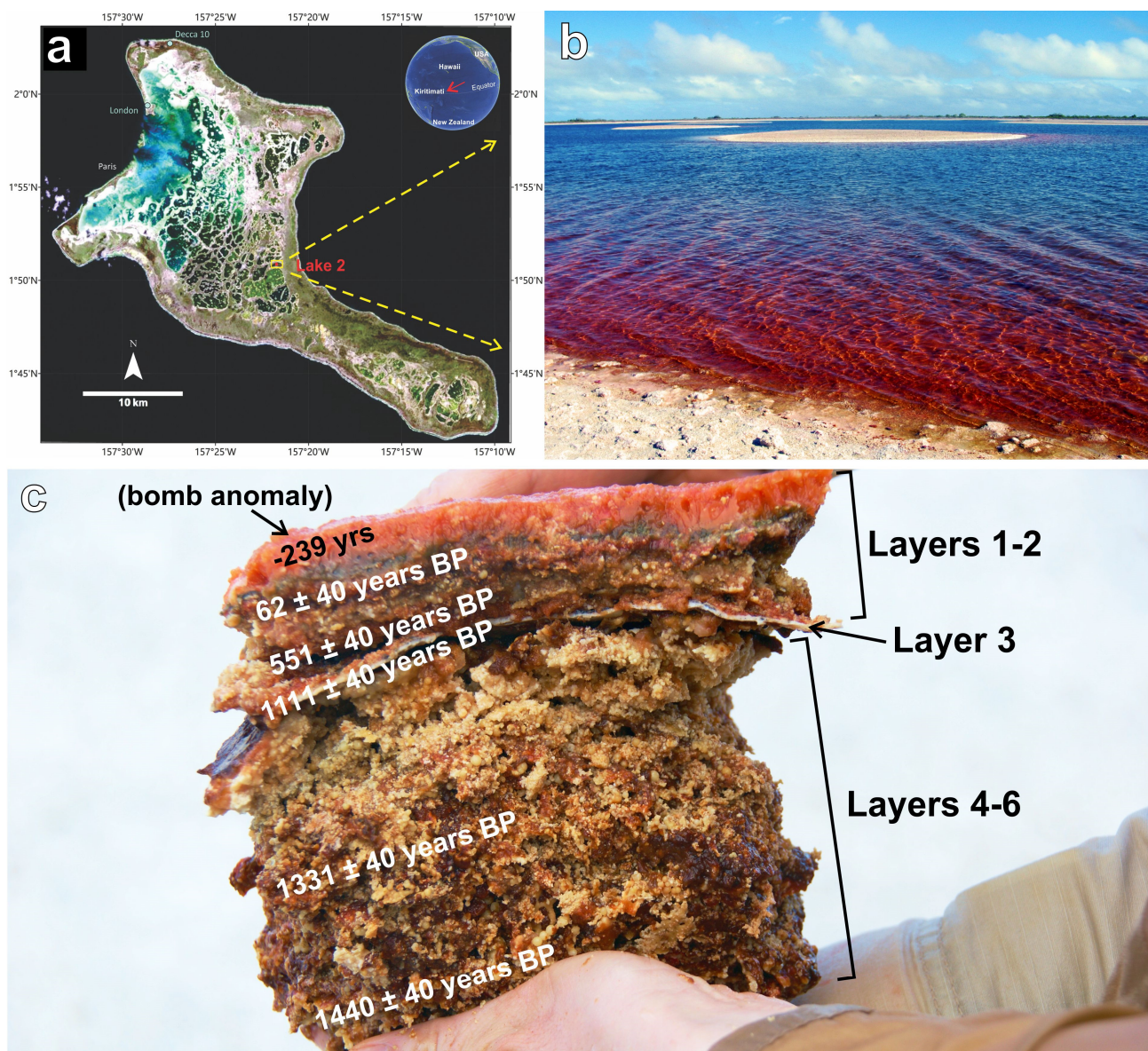


Figure 1. (a) General location of Kiritimati atoll in the Pacific Ocean and its satellite image, showing reticulate distribution pattern of the lakes (red dot: sampling site, Lake 2); (b) general view of hypersaline Lake 2 in Kiritimati; (c) the microbial mat sampled for this study, with clear color-zonation; note the whitish mineral crust (Layer 3) separating the upper fresher part of the mat from the older, more mineralized layers. ^{14}C dates of carbonate particles were measured by Blumenberg et al. [30]. (BP: before present, i.e., before 1950, before the start of the worldwide nuclear bomb tests; note the significant deviation (bomb anomaly) of 239 yrs at the topmost of the mat, as result of the bomb tests).

2.2. Previous ^{14}C Dating of the Studied Material

Blumenberg et al. [30] provided ^{14}C ages of the studied mat, shown in Figure 1. The downwards increase in age suggests that the dating is consistent. However, the location in an atoll with a substrate of coral reef limestone [27] suggests that the ^{14}C signal could be affected by a marine reservoir and local hardwater reservoir effects, as typically occurs in atoll settings [31,32], which was not taken into account by Blumenberg et al. [30]. Studies that considered the marine reservoir effect in Kiritimati showed that a ^{14}C correction factor of 39 ± 56 years produces good correlations with U/Th ages [33,34]. In addition, the distance of the studied Kiritimati Lake 2 from the coast (Figure 1) and its persistent hypersalinity indicate disconnection from seawater, allowing equilibration

of C reservoir in lake water with atmospheric CO₂ [29]. A hardwater reservoir effect could be another potential modifier of the ¹⁴C ages of Kiritimati mats, if groundwaters from the underlying coral reefs seeped into the mat-bearing lakes. Hydrological data led Arp et al. [27] to suggest that surface or groundwater influx could have been possible in Kiritimati hypersaline lakes, however their stable O and C isotope values also showed that the water of these lakes mainly derives from highly evaporated marine water. Additional ¹⁴C analyses were obtained for corals from the surroundings of Lake 2, obtaining ages of ca. 2500 years BP (unpublished own data), significantly older than the ages obtained by Blumenberg et al. [30] for the mat studied here, supporting that the ¹⁴C signature of the studied microbial mats is not strongly influenced by that of old underground water. Therefore, although a minor hardwater effect is possible, we will use here the ¹⁴C ages obtained by Blumenberg et al. [30], as for the aim of this study the absolute age values are not directly relevant, but rather the downwards increase in age and the relative differences between ages of different mat layers.

2.3. Preparation for Histological Thin Sections

For the preparation of histological thin sections, samples were dehydrated with a graded ethanol series. Afterwards, mat samples were embedded in LR White resin (medium grade, London Resin Company Ltd., Reading, UK). The embedded samples were cut with a microtome saw (Leica SP1600) to a thickness of c. 100 µm, mounted on glass slides using Biomount mounting medium (Electron Microscopy Sciences, Hatfield, PA, USA). Thin sections were studied under petrographic and fluorescence microscope (Zeiss Axiophot, Jena, Germany).

2.4. Preparation for the Electron Microscope

To observe the mineral fraction of the microbial mat under field-emission scanning electron microscopy (FE-SEM), the organic matter of the samples was removed through oxidation with NaOCl [35]. Each sample from individual mat layer was immersed in 6% NaOCl, changing the solution every 12 h for several days, until no traces of organic matter were visible. The remaining mineral particles were washed with distilled H₂O until pH was neutral, and then dried. Mineral particles were mounted on SEM sample holders and sputtered with Pt/Pd (14.1 nm for 5 min, using a Leica EM QSG100) and then observed in a FE-SEM (Zeiss Leo Gemini 1530).

2.5. Mineralogical and Elemental Analyses

Various non-destructive methods were used for investigating the composition of the microbial mat minerals. For detailed elemental mapping and point analyses, the FE-SEM microscope was used, coupled with an Oxford Instruments INCA x-act energy dispersive X-ray spectrometry (EDX) detector. In addition, a micro X-ray fluorescence (µ-XRF) device was applied to obtain elemental distribution images of thin sections. The analyses were conducted with a Bruker M4 Tornado instrument equipped with an XFlash 430 Silicon Drift Detector. Measurements (spatial resolution = 25–50 µm, pixel time = 8–25 ms) were performed at 50 kV and 400 µA at a chamber pressure of 20 mbar.

Mineralogical identification was conducted using Raman analyses. Raman spectra were collected using a WITec alpha300R coupled ultra-high throughput spectrometer. Before analysis, the system was calibrated using an integrated light source. The experimental setup included a 405 nm laser, 10 mW laser power, a 100× long working distance objective with a numerical aperture of 0.75, and a 1200 g mm⁻¹ grating. This setup had a spectral resolution of 2.6 cm⁻¹. The spectrometer was centered at 1530 cm⁻¹, covering a spectral range from 122 to 2759 cm⁻¹. The 405 nm laser was chosen to reduce fluorescence effects [36]. Each spectrum was collected by two accumulations, with an acquisition time of 60 s. Raman spectra were processed with the WITec project software.

2.6. Extraction and Derivatization

Two different types of lipids were extracted and analyzed separately in this study: the lipids present in the organic matrix of the mat (here termed 'freely extractable lipids') and those present within the carbonate precipitates of the mat (here termed 'carbonate-bound lipids'). Both lipid types were analyzed for each layer of the microbial mat. A small portion (5–20 g) of each layer was sampled and freeze dried. After freeze-drying, samples were homogenized (not powdered) and extracted by 4 × 50 mL dichloromethane/methanol (3:1; *v:v*) (10 min ultrasonication) to obtain the freely extractable lipids. The resulting extraction residue was decalcified using 37% HCl and was again extracted as described above to obtain the carbonate-bound lipids.

To make carboxylic acids GC-amenable, a mixture of trimethylchlorosilane (TMCS)/MeOH (1:9, *v:v*) was added to lipid extracts (5% aliquot of the lipids from the previous layer division and 25% aliquot from layers 2b, 4a and 4b). Both freely extractable and carbonate-bound lipids were reacted at 80 °C for 60 min. The resulting carboxylic acid methyl esters and the neutral lipids (including *n*-alkane and hopanoid hydrocarbons) were extracted from the reaction mixture by vigorous shaking with 3 × 1 mL *n*-hexane. The extracts were combined and evaporated to near-dryness under a gentle N₂ flow, re-dissolved in *n*-hexane, and analyzed by gas chromatography-mass spectrometry (GC-MS).

To make alcohols (including sterols and hopanols) GC-amenable, all aliquots (identical amounts were used as showed above) of lipid fractions were silylated using BSTFA (N,O-bis(trimethylsilyl)trifluoroacetamide) containing 5% (*v:v*) trimethylchlorosilane (TMCS) as a catalyzer (heated at 70 °C for 60 min). The resulting trimethylsilyl (TMS-) derivatives were dried, and re-dissolved in *n*-hexane, and analyzed by gas chromatography-mass spectrometry (GC-MS).

GC-MS analyses were conducted using a Thermo Fisher Trace 1310 GC coupled to a Thermo Fisher Quantum XLS Ultra MS as described elsewhere [37]. *N*-Icosane-D₄₂ was used as an internal standard for quantification.

2.7. Compound-Specific Stable Carbon Isotopes (GC-C-IRMS)

Compound-specific stable carbon isotope ratios were measured for microbial lipids (i.e., FAs and hopanoids), hydrocarbons and sterols (including freely extractable and carbonate-bound lipid fractions) in the studied microbial mat. In order to interpret the general trend of isotope signatures, layers 1, 3, 5 and 6 were chosen and analyzed, thus including data from the upper, middle and lower parts of the mat, respectively (see description of the mat in Section 3 Results section). Analyses were conducted using a Thermo Scientific Trace gas chromatograph (GC) coupled to a Delta Plus isotope ratio mass spectrometer (IRMS) as described elsewhere [38].

3. Results

3.1. Macroscopic Description of the Mat Layers

The studied microbial mat has a thickness of c. 10 cm and it is divided in two main parts (composed of mineral particles within an organic matrix, Figures 1c and 2) and separated by a thin yet conspicuous and continuous mineral crust (Figures 1c and 2). The upper part is composed of two layers (1–2, c. 3 cm thick, Figures 1c and 2), which have a cohesive appearance, sticking together when handled, due to abundant and relatively fresh organic material. This organic matrix shows bright orange, green and brown colors with transparent or whitish mineral particles, rare and scattered in the top layer 1 and more abundant in layer 2. The lower part of layer 2, closer to the underlying mineral crust has been termed layer 2b and analyzed separately using organic geochemical techniques (Figure 2). The mineral crust that separates the two main parts of the mat is here termed layer 3 and it is thin (1–2 mm) although laterally very continuous (Figures 1c, 2, 6 and 7). The lower part of the mat (c. 7 cm thick) is more friable, having a crumbly appearance, due to the rarer and poorly preserved organic material and more abundant mineral particles, producing brown and beige colors (Figures 1c and 2). This lower part is subdivided in three

main layers (4–6, Figures 1c and 2). The top parts of layer 4, closer to the mineral crust, have been also analyzed separately using organic geochemical techniques, as layers 4a (dark brown color and immediately below the crust) and 4b (below 4a and with a lighter beige color) (Figure 2). The ^{14}C ages of the mat [30] show that its upper (and thinner) part was formed approximately in the last 1100 years (62 ± 40 years BP for layer 1, 551 ± 40 years BP for layer 2 and 1111 ± 40 years BP for layer 3; Figure 1c), whereas the lower (and thicker) part was formed approximately in the previous 350 years (1331 ± 40 years BP for layer 5 and 1440 ± 40 years BP for layer 6; Figure 1c).

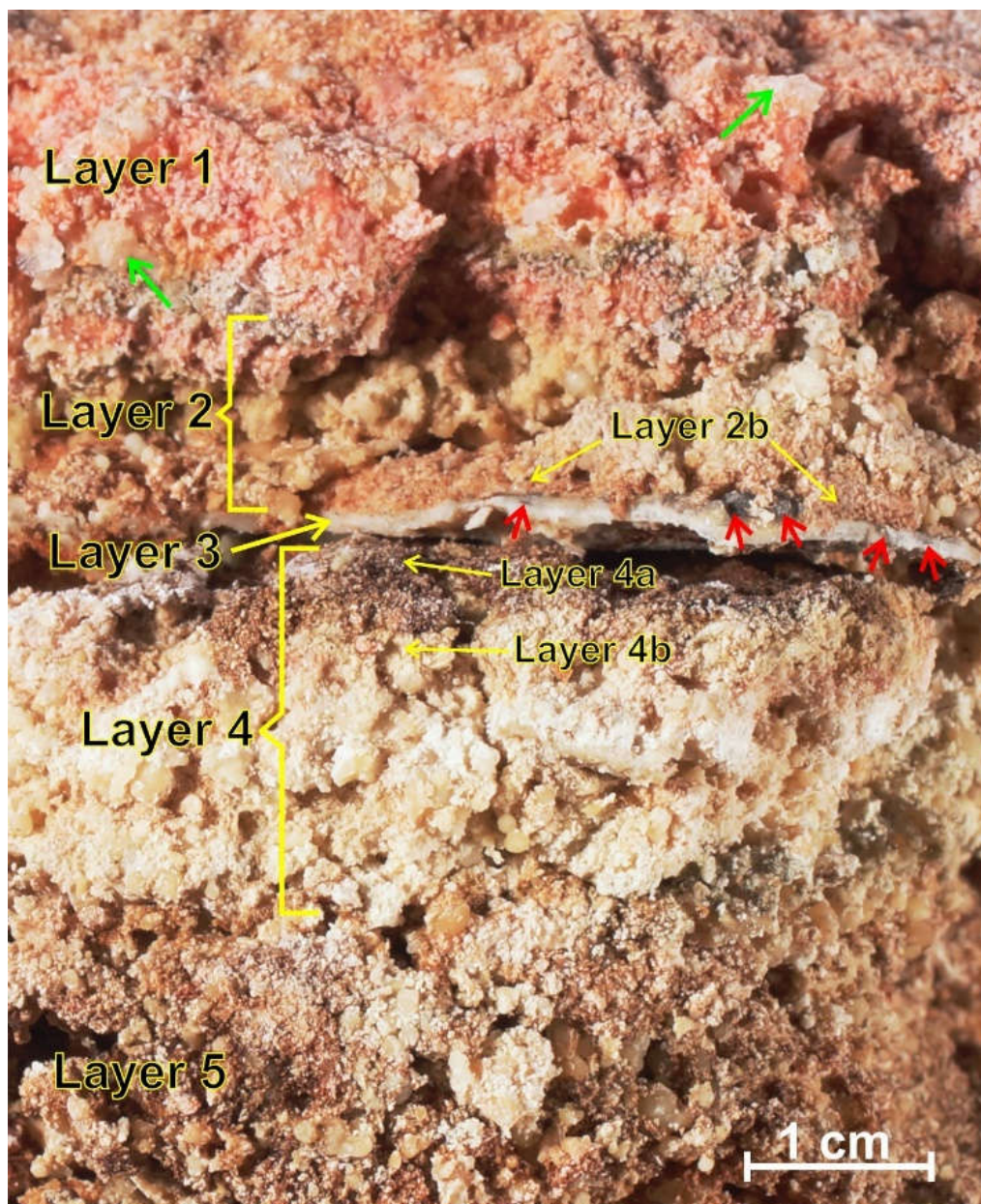


Figure 2. Close-up picture of frozen microbial mat sample studied in this work (compare with Figure 1c). Green arrows point to transparent gypsum crystals, which occur only in the uppermost layer. Note common beige, irregular to subspherical, carbonate particles, more abundant downwards in the mat. Red arrows point to dark inclusions within the thin mineral crust of layer 3.

3.2. Microscopic Observation of Mat Layers

The cohesive appearance of the upper part of the mat (layers 1–2) is due to its abundant and fresh organic matter. Under the microscope, this organic matter is mainly seen as a dense reticulate microstructure formed by a net of intertwined delicate fibers of extracellular polymeric substances (EPS, Figure 3a,b). Within this network of EPS fibers, the dominant microorganisms observed are colonies of coccoid cyanobacteria and less abundant filamentous cyanobacteria (Figure 8a), as is typical in hypersaline Kiritimati mats [27,28,39]. Locally, miliolid foraminifera are also observed in layer 1. Scattered mineral particles occur within these layers. Local idiomorphic gypsum crystals occur in layer 1 (Figures 2 and 4a), however the predominant particles are composed of aragonite [27,40]. Two different types of aragonitic particles are observed in layers 1–2: (a) relatively abundant small (<2 mm in diameter) subspherical particles with a crystalline fibrous-radial internal structure and typically growing around a micritic nucleus (Figures 3a,b and 4a,d,e; cf. ‘spherulites’ of Arp et al. [27], or ‘non-laminated ooids’ of Suarez-Gonzalez and Reitner, [40]); (b) less abundant irregular micritic particles with a micropeloidal internal texture (Figure 4c). When various subspherical particles are very close to each other, they tend to coalesce together during their growth, forming composite particles (Figures 3a,b and 4a,e). These two types of aragonitic particles, subspherical and irregular micritic, are also the main mineral components of the lower layers 4–6 (Figures 3d, 4b,f and 5), but layer 3 shows a markedly different composition.

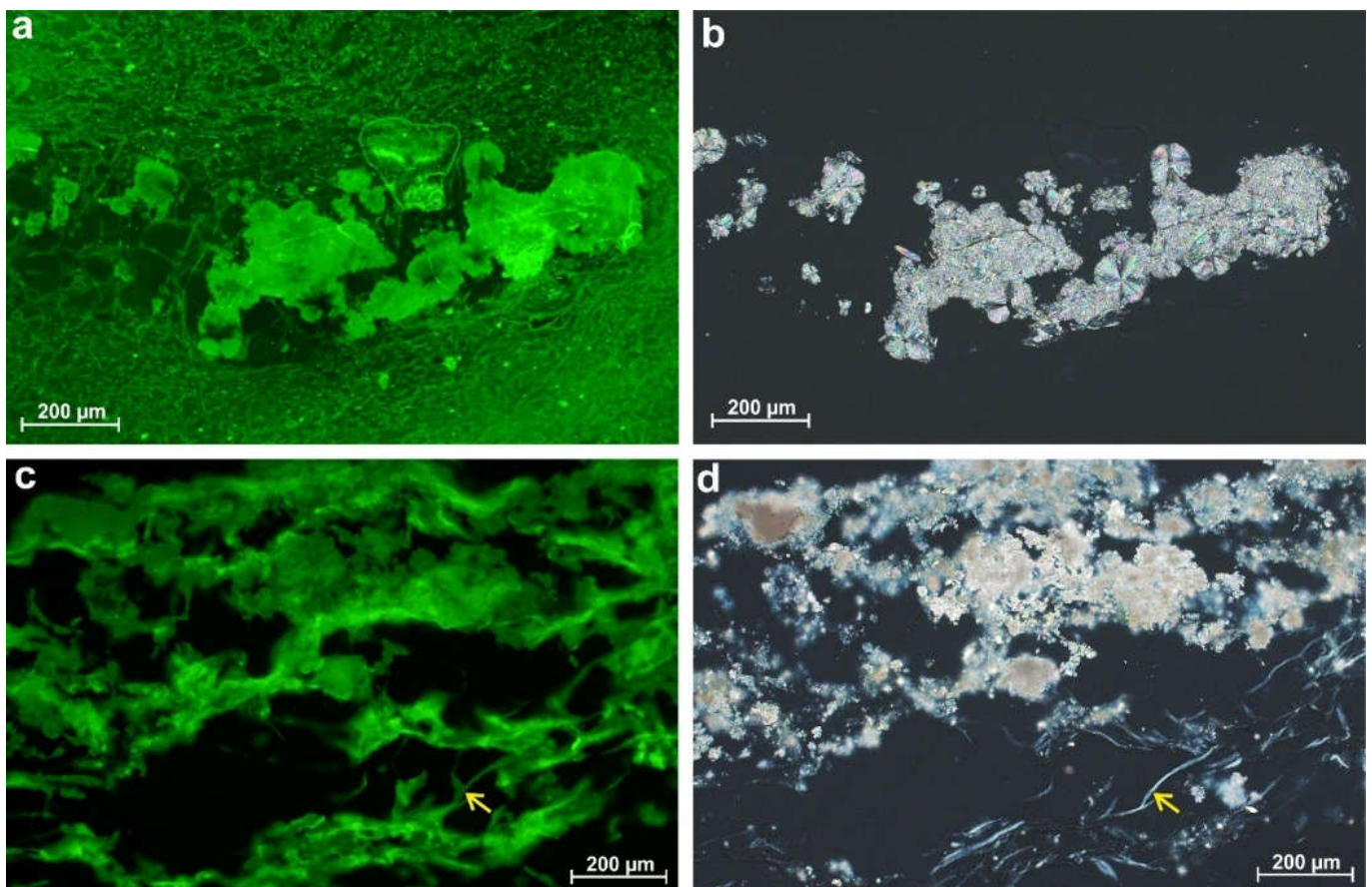


Figure 3. Different preservation of the exopolymers (EPS) of the organic matrix of the mat. (a,c) Photomicrographs taken with fluorescence microscope. (b,d) Same areas as a, c, however seen with cross-polarized light. (a,b) Carbonate precipitates from the topmost Layer 1, within a dense reticulate net of intertwined delicate fibers of younger and fresher EPS, which show no birefringence (black color in (b)) with cross-polarized light. (c,d) Carbonate precipitates from the lowermost Layer 6, forming in a less dense and more porous matrix of older EPS with a laminated microstructure of coarser individual EPS fibers, which show birefringence (yellow arrow in (d)) with cross-polarized light.

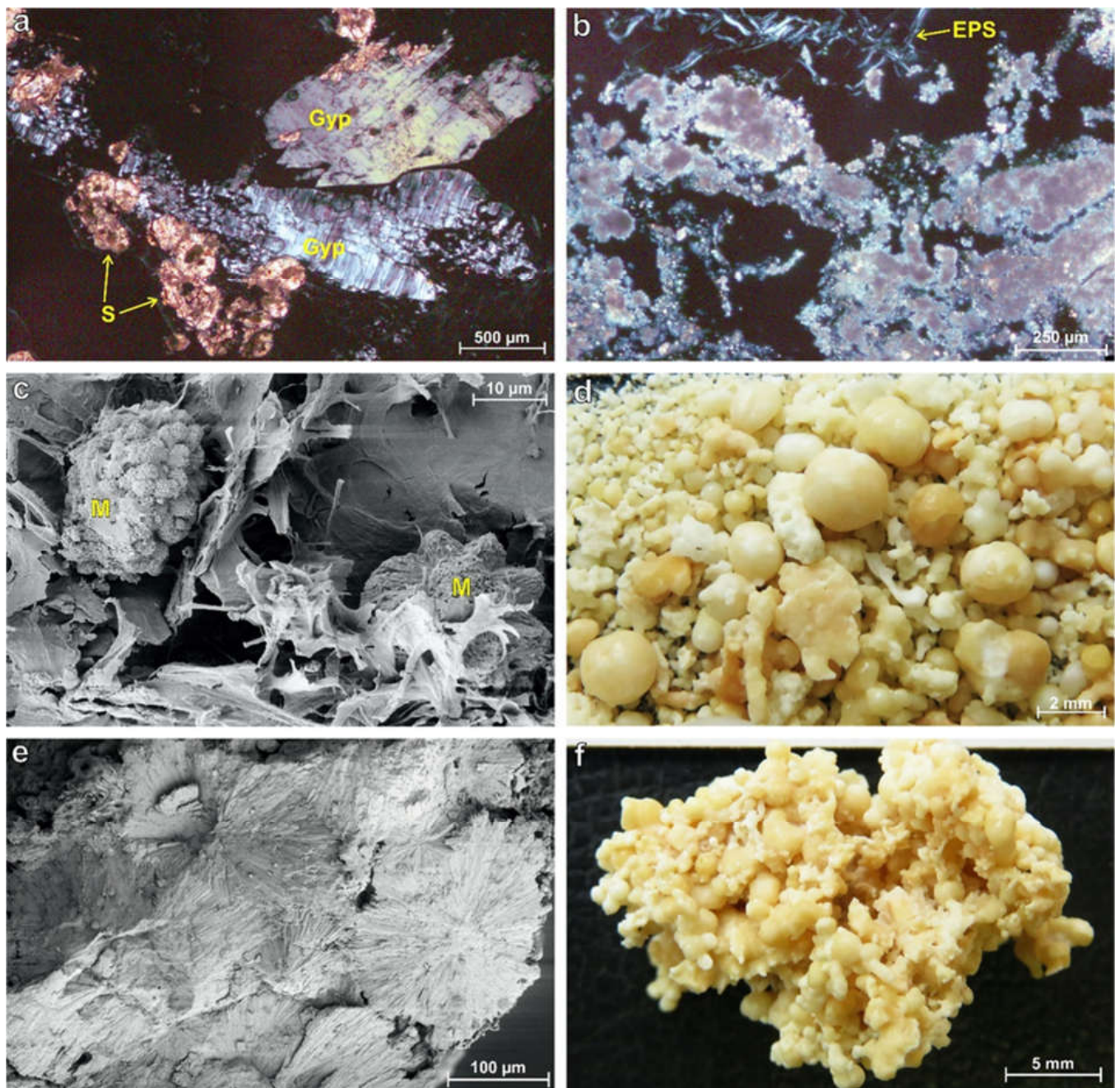


Figure 4. Mineral precipitates observed within the studied microbial mat: (a) Cross-polarized light photomicrograph of gypsum crystals (Gyp) and subspherical aragonite particles (S) from Layer 1; (b) Cross-polarized light photomicrograph of irregular micritic aggregates from Layer 6, showing their micropeloidal internal texture. Yellow arrow points to thick and birefringent EPS threads; (c) SEM image of an irregular micritic aggregate from Layer 1, showing a detail of its micropeloids (M), formed by intergrown bundles of aragonite needles, and completely surrounded by a matrix of EPS, within which they precipitate; (d) Close-up picture of the loose mineral particles extracted from Layer 2 after complete removal of the organic matter. Note the presence of both subspherical particles and irregular aggregates; (e) SEM image showing a section of coalesced subspherical particles from Layer 2. Note their fibrous radial structure formed by aragonite needles; (f) Large irregular carbonate aggregate from Layer 4 after complete removal of organic matter. Note that it is formed by the coalescence of both subspherical particles and micritic aggregates. Large complex aggregates are typical from the lower older layers of the mat (compare with the younger precipitates of Figure 4d).

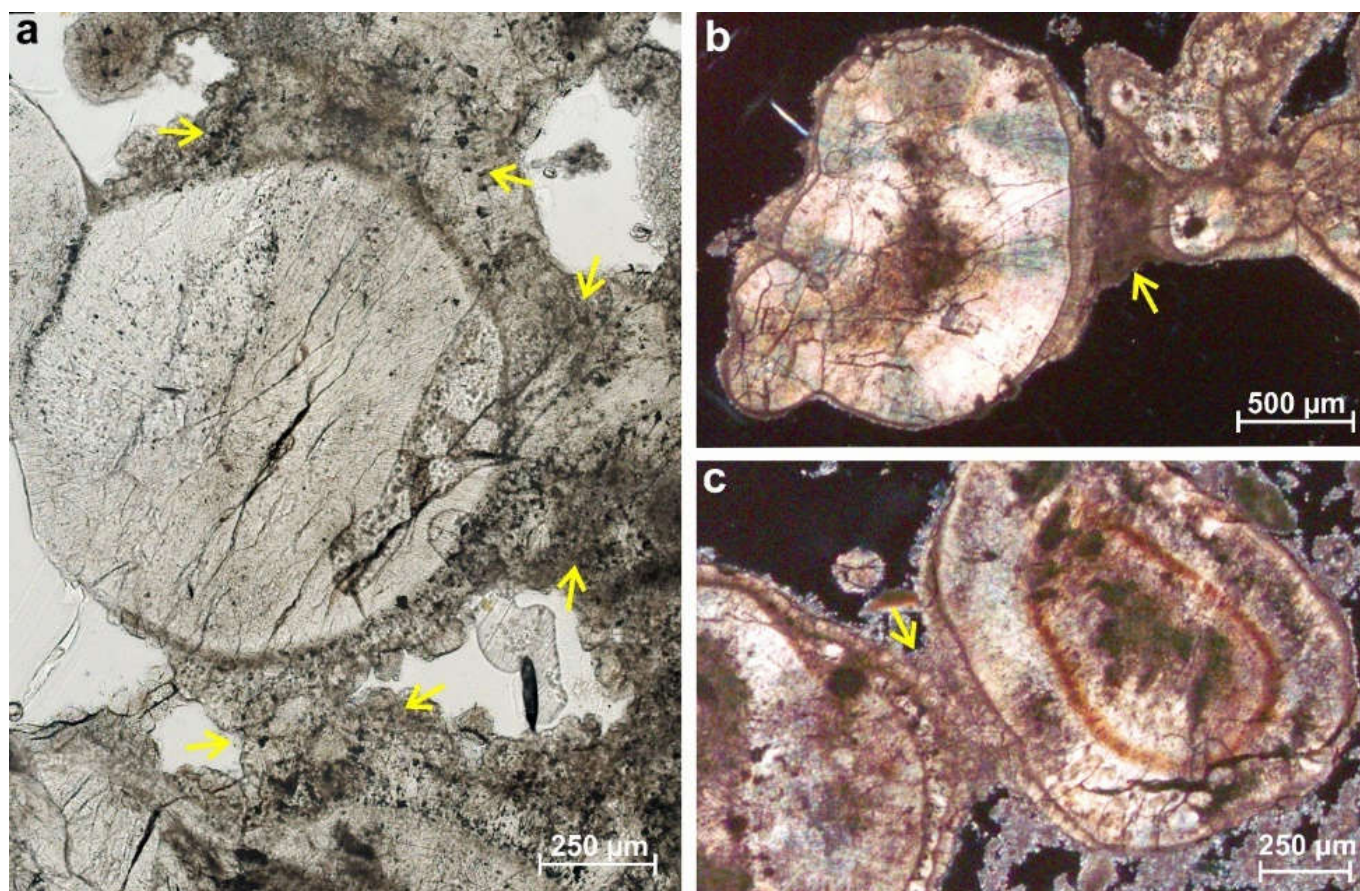


Figure 5. Photomicrographs of subspherical particles of the upper part of layer 4, merged together by micritic aggregates with meniscus morphology: (a) Transmitted light photomicrograph; (b,c) Cross-polarized light photomicrograph.

Layer 3 is a thin but laterally continuous mineral crust with features not common in other microbial mats previously described from Kiritimati [26,27,41]. With the naked eye, this crust shows white-beige colors with darker inclusions, and it generally has a flat bottom and domed top (Figures 2 and 6). Microscopically, the crust is composed of up to seven superposed laminae with a fibrous-radial internal texture, formed by long mineral needles (Figures 6–12). The two lowermost laminae are flat, however the rest are botryoidal in shape (Figures 6–9). The lower laminae are thin (100–500 μm) and laterally discontinuous (Figures 6c and 7a). The upper laminae are thicker (up to 1 mm) and laterally more continuous (Figures 6c and 7a). The mineralogical and elemental composition of the crust has been studied in detail. Raman spectra of the long mineral needles that compose it exhibit wave numbers (206, 702 and 1086 cm^{-1}) characteristic of aragonite (Figure 6b). No organic remains were detected within these aragonite crystals. In addition, $\mu\text{-XRF}$ elemental maps of the crust show that the main cations present are Ca and Sr (Figure 7). Minor and patchy occurrence of Mg is related with local miliolid foraminifers at the base of the crust (Figure 7, see further description below). EDX point measurements of the crust were compared with an aragonite standard, showing Sr values calculated between 8000–10,000 ppm, which is characteristic for aragonite precipitated in seawater equilibrium.

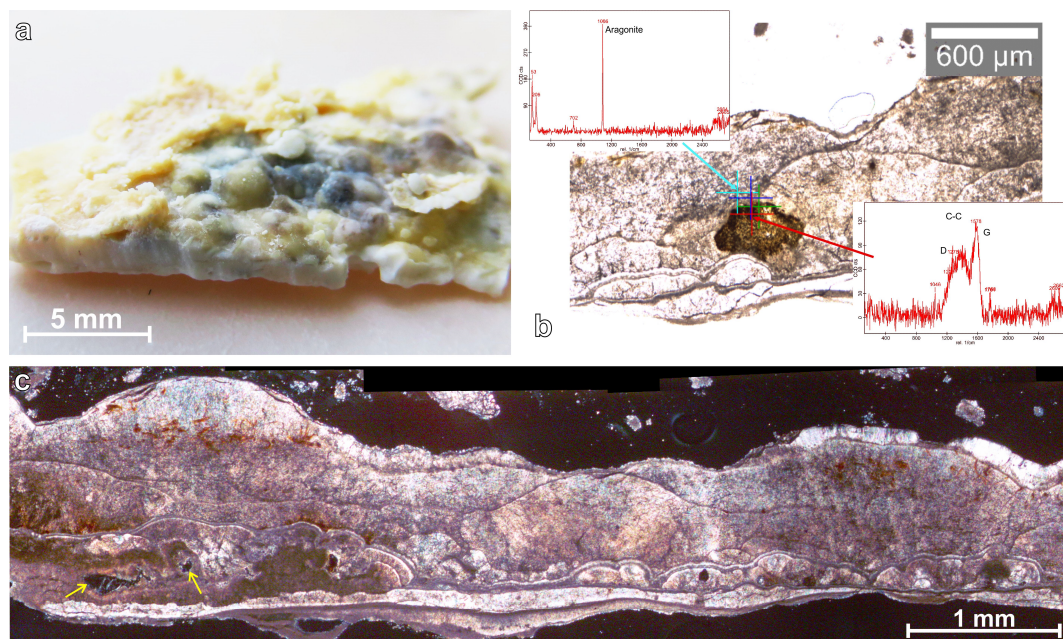


Figure 6. Thin mineral crust of layer 3: (a) Close-up picture of the mineral crust of Layer 3 after complete removal of organic matter. Note the botryoidal upper surface of the crust and its local dark color; (b) Transmitted light photomicrograph of the thin crust of layer 3 with two Raman spectra from the crust. The upper left one shows the dominant aragonitic composition of the crust (as in most precipitates of the Kiritimati mats, cf. [27,40]). No traces of organic carbon are detected. In contrast, the lower right spectrum shows the organic composition of a dark inclusion rich in coccoid cyanobacteria (see Figure 8). The spectrum has a very broad D-band (disordered) with an unclear main peak (around wave number 1300). The G-band (graphite band) has wave number 1578; (c) Cross-polarized light photomicrograph of a thin section of the mineral crust of Layer 3, showing its internal structure, composed of several superposed laminae of botryoidal carbonate, indicating different precipitation episodes. Yellow arrows point to cavities within the crust, filled by organic matter.

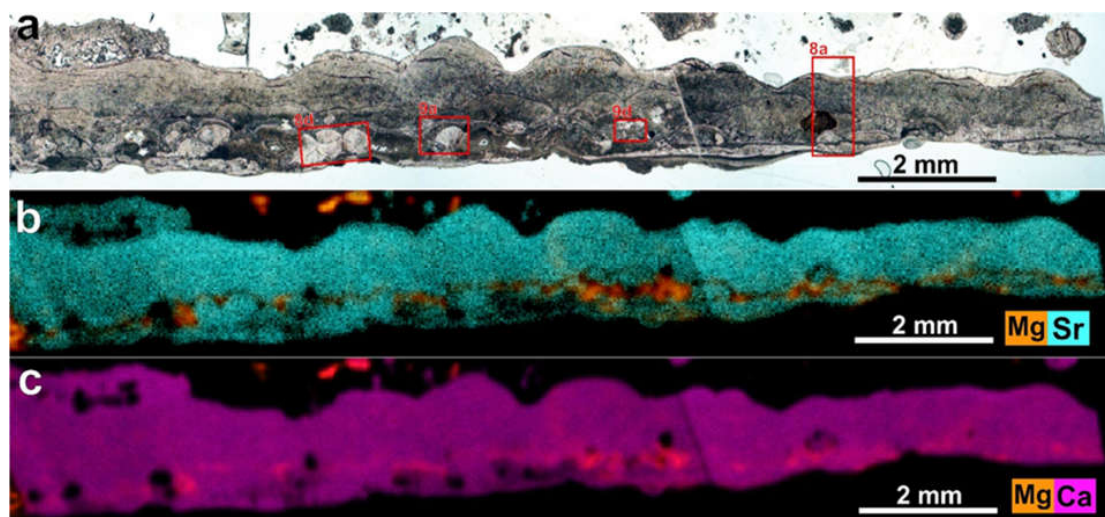


Figure 7. Elemental distribution within the thin mineral crust of layer 3: (a) Transmitted-light photomicrograph of the thin mineral crust. Red rectangles mark the position of Figures 8a,d and 9a,d; (b,c) μ -XRF maps of Ca, Mg and Sr within the crust, showing the high abundance of Sr, consistent with its aragonitic composition [42]. Local abundances of Mg correspond to scarce miliolid foraminifera occurring at the base of the crust (Figures 9d and 12b). See further descriptions in the text.

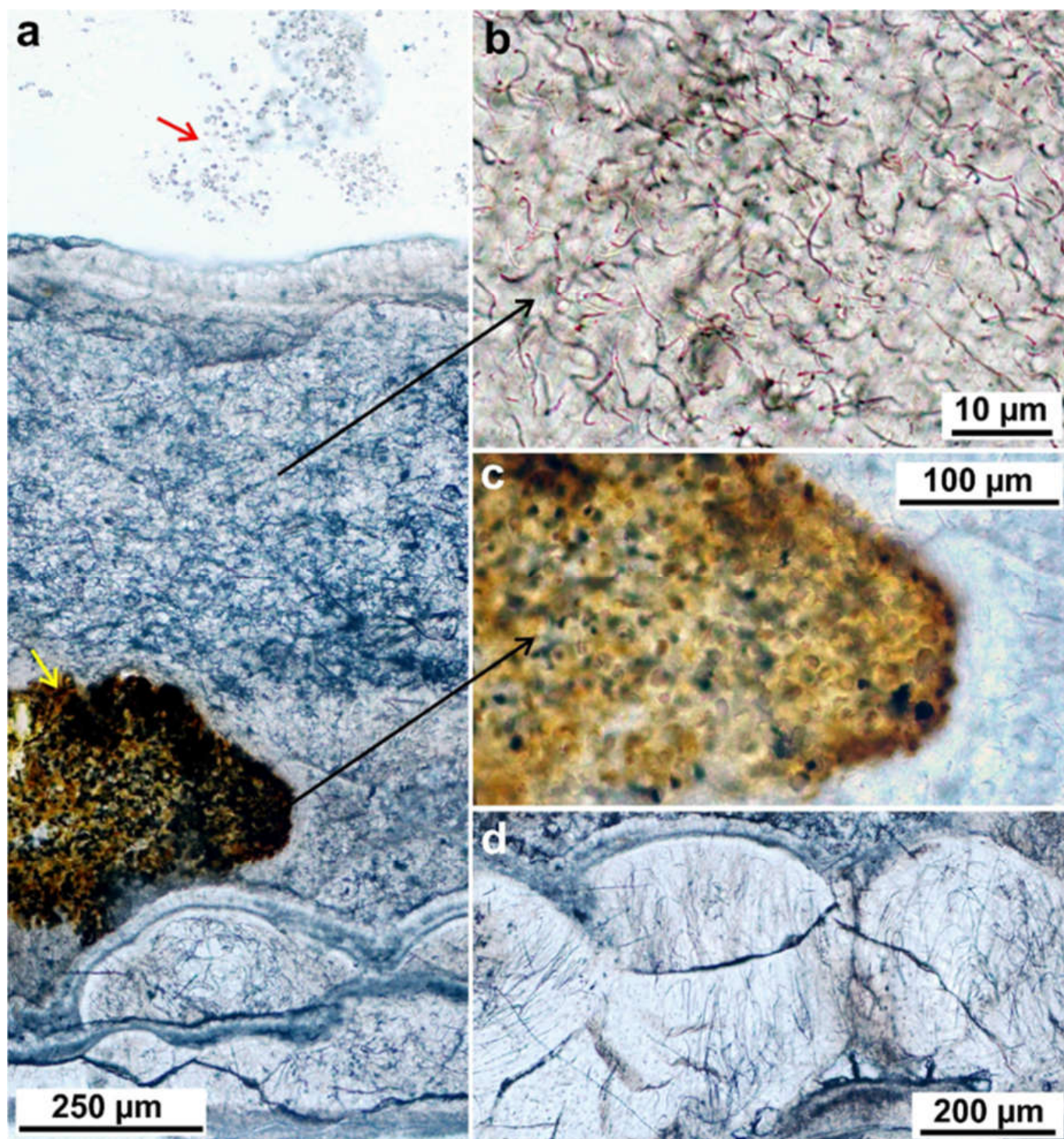


Figure 8. Detailed transmitted-light photomicrographs of the thin mineral crust of layer 3: (a) Vertical transect of the crust (see location in Figure 7a). Red arrow points to a colony of coccoid cyanobacteria in the overlying layer 2. Yellow arrow points to a fossil colony of coccoid cyanobacteria rich in organic matter (see Figure 6b) and entombed within the crust. See detail in (c); (b) Detail of the upper part of the crust, showing that its cloudy appearance is caused by extremely abundant molds of curved filaments, many of them showing branching; (c) Detail of the boundary of the colony of coccoid cyanobacteria entombed within the crust; (d) Detail of small aragonite botryoids (see location in Figure 7a), which include tufts of filaments. Note that the shape and orientation of the botryoids mimics that of the tufts.

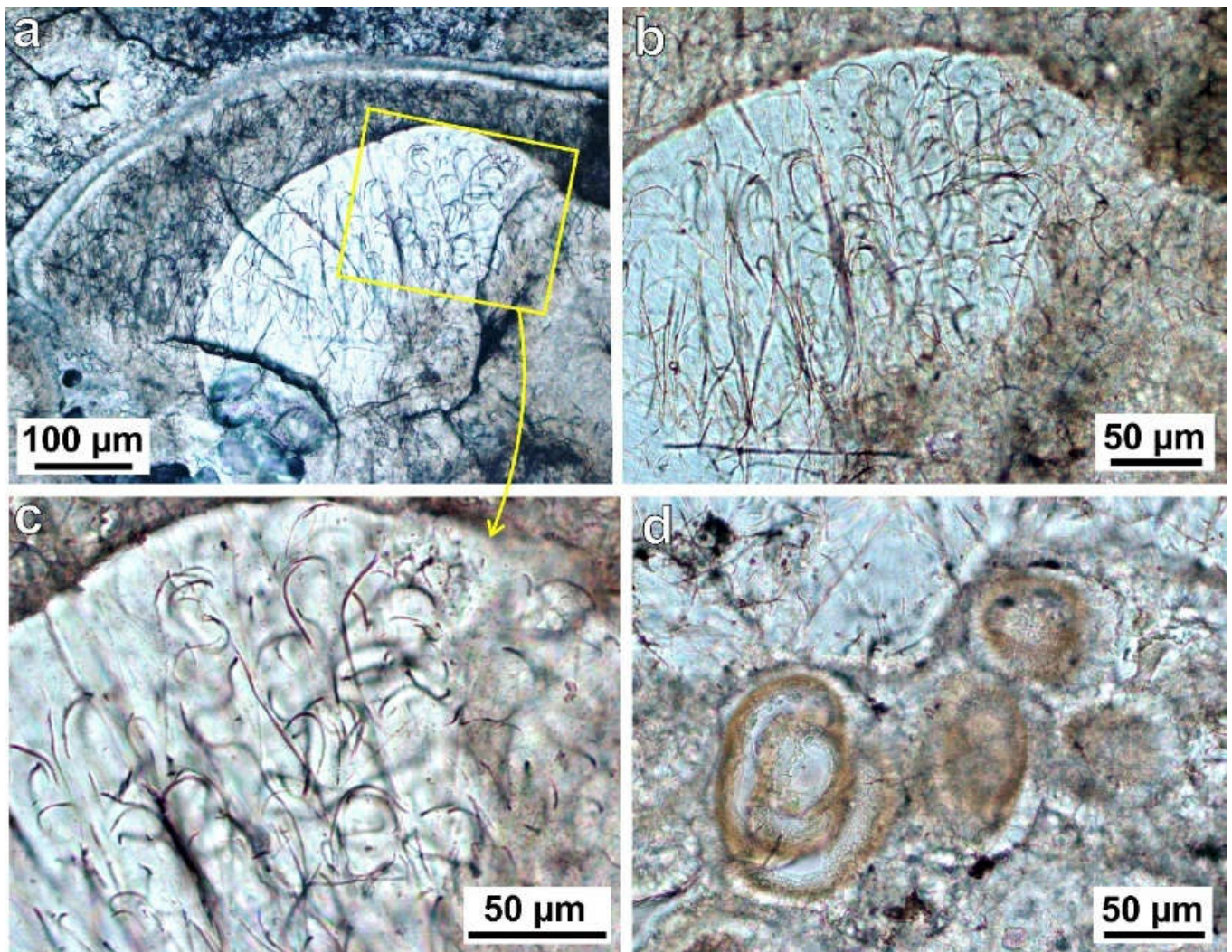


Figure 9. (a) Transmitted light photomicrograph showing a detail of a carbonate botryoid from layer 3 (see location in Figure 7a). Note the fibrous-radial internal texture and the presence of very abundant curved dark filaments. The cloudier aspect of the outer part is due to a higher abundance of dark filaments. (b) Detailed transmitted light photomicrograph of a botryoid from layer 3 including abundant curved filament tufts, whose morphology seems to be mimicked by the mineral botryoid. (c) Detail of (a), showing the curved dark filaments preserved within the botryoid. (d) Detailed transmitted light photomicrograph of miliolid foraminifers preserved within the lower part of the crust. See location in Figure 7a.

The layer 3 crust includes abundant large pores filled with residual organic matter (mainly EPS, Figures 6, 8 and 12), which generate the darker areas observed macroscopically within the crust (Figures 2 and 6). Some of the inclusions are filled by entombed colonies of coccoid cyanobacteria (Figure 8a,c). Raman spectra of these colonies show that they are mainly organic, with a typical broad D-band with many subordinate peaks (main peak 1278) and G-band with 1579 as the main wave number (Figure 6b). The wave number 1046 could be due to nahcolite (NaHCO_3), which is characteristic of hypersaline environments, however this should be tested with further analyses. Other organic remains within layer 3 are molds of filamentous microbes and diatoms, which are ubiquitous throughout the crust, enclosed within the fibrous crystalline structure of the botryoids (Figures 8–12). Miliolid foraminifera have also locally been observed within the lower part of the crust, which contrast in elemental composition with the rest of the crust, given their high-Mg-calcite mineralogy (Figures 7, 9d and 12b). The molds of filamentous microbes are long (up to 200 μm) but thin (<5 μm , and typically ~1 μm) and very abundant, thus being easily observed under the petrographic microscope

(Figures 8–11). In some of the botryoids they are so abundant that they provide a cloudy appearance to the aragonite (Figures 8a, 9a and 11a). Generally, the filaments are erected and curved, forming tufted structures that mimic the shape of the aragonite botryoids (Figures 8a,d and 9a–c) and some of them seem to have branching structure (Figure 10b–d). These filaments show bright fluorescence (Figure 11). Locally, at the top part of the crust, larger filaments (up to 500 μm long and 40 μm thick), with brownish color in thin section and no fluorescence, are also observed, showing irregular orientation, from vertical to horizontal, apparently not associated with the botryoid structure (Figures 6c and 11). Contrarily to the filament molds, diatom molds are much smaller (up to 50 μm long and 10 μm wide) and thus not observable in the thin section, however are ubiquitously observed under SEM (Figure 12d). Both filament and diatom molds are either empty (preserved as porosity) or filled by carbonate with only local preservation of the original EPS (Figure 12d,f).

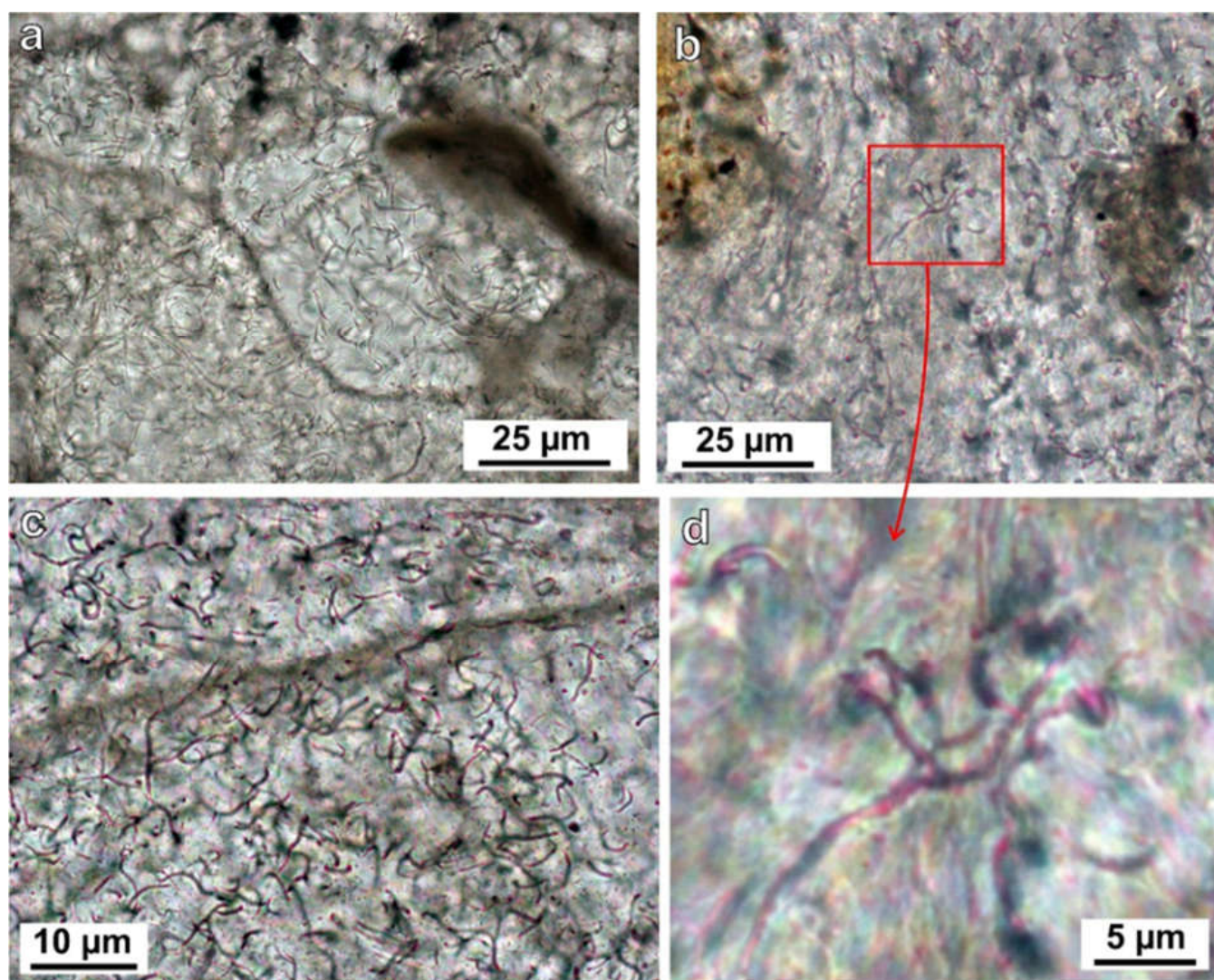


Figure 10. Thin filaments preserved within the crust of layer 3: (a) Detailed transmitted light photomicrograph of the dense framework of curved filaments preserved within an aragonite botryoid of the crust. Note that most filaments are $\sim 1 \mu\text{m}$ thick or less; (b,c) Transmitted light photomicrograph of the filaments clearly showing their curved morphology, some of them with branching; (d) Detail of (b) clearly showing the curved and branching morphology of the filaments, which resemble hyphal branching networks of Actinobacteria or fungi, as well as the local swelling knots, which are comparable with reproductive structures like spores. Compare with figures in Li et al. [43].

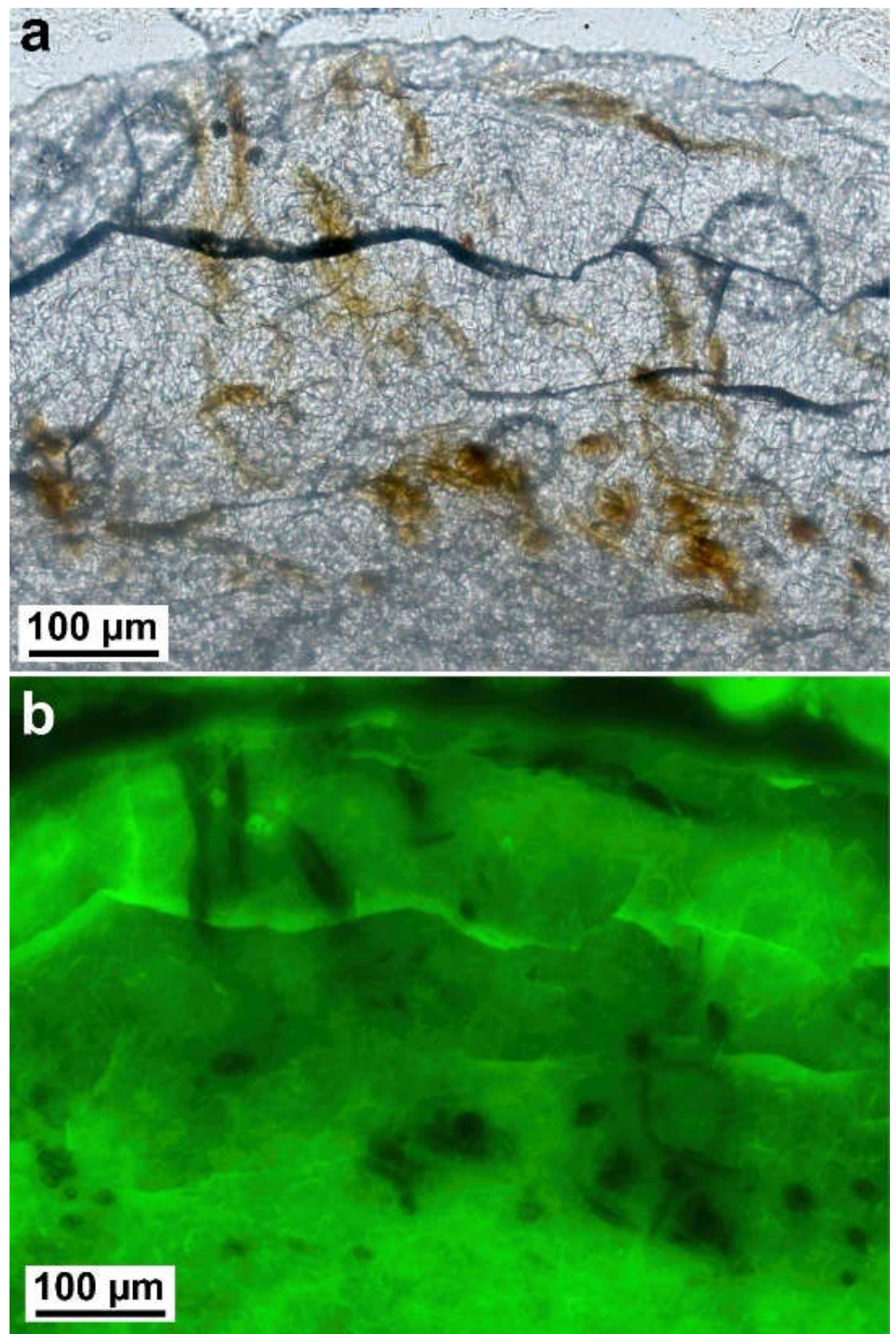


Figure 11. Different filaments in the upper part of the thin mineral crust of layer 3: (a) Transmitted light photomicrograph and; (b) Fluorescence photomicrograph of the same area. Note the cloudy appearance of the botryoid, due to the high abundance of small filament molds, which are highly fluorescent, and which contrast with the larger brown filament molds that are not fluorescent. Some of these larger filaments seem to penetrate the crust from its upper surface.

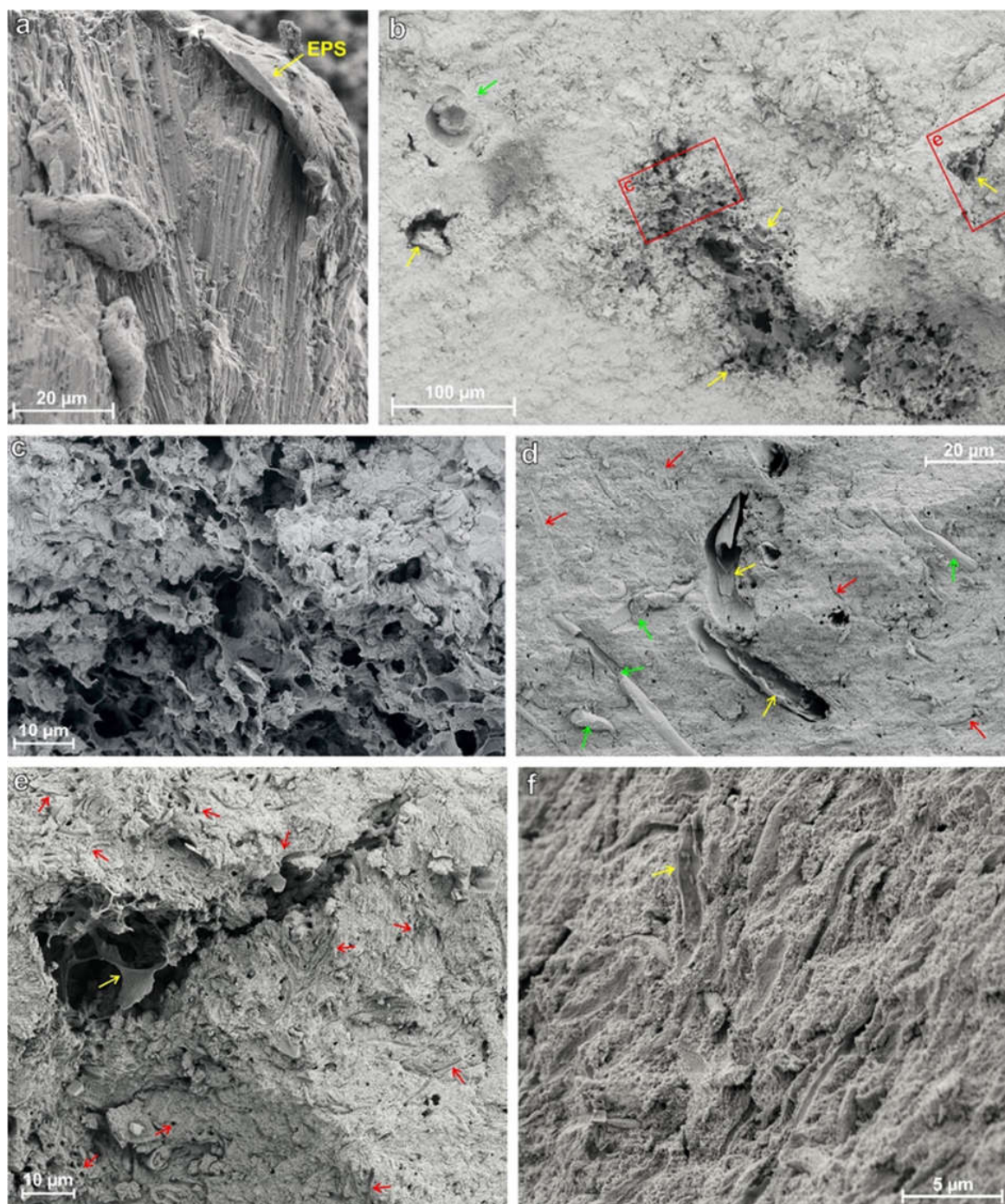


Figure 12. SEM images of the thin mineral crust of layer 3: (a) Fibrous-radial structure of a carbonate botryoid from layer 3, formed by aragonite needles, and covered by a thin film of EPS; (b) A freshly-cut section of layer 3, showing irregular and partially-filled cavities (yellow arrows) and a section of a foraminifer (green arrow). Red rectangles mark the position of (c,e); (c) Detail of (b), showing the EPS matrix that infills the cavities observed within the mineral crust of layer 3; (d) Close-up view of a freshly-cut section of the mineral crust of layer 3, showing molds of diatoms (green and yellow arrows) and much more abundant small filaments (red arrows) included within the mineral crust. Most diatom molds are filled by carbonate (green arrows), however locally others are partially empty, with some remains of EPS (yellow arrows); (e) Detail of (b), showing a cavity filled with EPS (yellow arrow) and ubiquitous filament molds. Red arrows only point to some locations with an important concentration of filaments, however many more can be observed throughout the image; (f) Close-up image of many filament molds. Yellow arrow points to a mold that partially preserves the EPS of the filament sheath.

Similar thin mineral crusts have not been observed in other modern Kiritimati microbial mats, however they occur in some of the subfossil mineralized mats, preserved as microbialites and occurring below the modern mats (Figure 13). Interestingly, the crusts in these examples also occur as thin yet laterally-continuous interruptions in accretion, around the middle part of the microbialites (Figure 13a,b), and they show the same layered botryoidal structure (Figure 13b–d). Furthermore, most botryoids of the crusts of these subfossil microbialites also have a cloudy appearance in thin section, due to very abundant filament molds, identical to those described in layer 3 of the studied microbial mat of Lake 2 (Figure 13c–f). Some of the filaments within the microbialite crusts are so well preserved that they even show the branching and segmented shaped of the original microbe (Figure 13f).

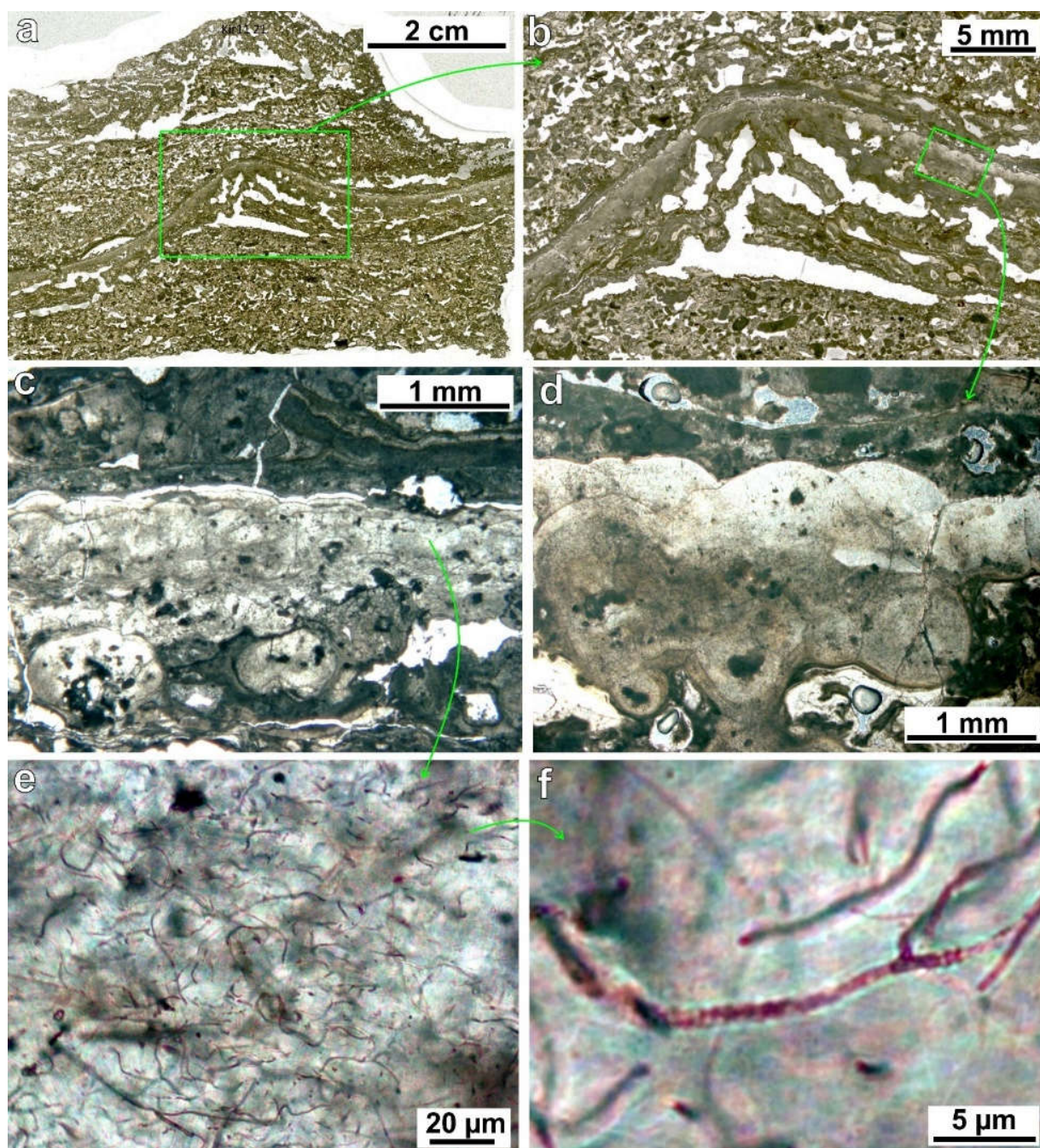


Figure 13. Thin mineral crust of subfossil microbialites from Kiritimati Lake 21 ($01^{\circ}57'45.63''$ N, $157^{\circ}19'53.03''$ W): (a) Transmitted light photomicrograph with an overview of the sample, clearly

showing the thin yet laterally continuous mineral crust interrupting the microbialite accretion, around the middle part of the sample; (b) Detail of (a) showing the botryoidal top of the thin mineral crust; (c,d) Detailed transmitted light photomicrographs of the thin mineral crusts. Note the complex laminated inner structure, composed of superposed botryoids, often with cloudy appearance, due to abundant filaments preserved within them; (e) Detail of the filaments preserved within the crust, with the same curved and branched structures as those preserved within the thin crust (layer 3) of the microbial mat of Lake 2, Figures 8–10; (f) Example of a filament that shows segmentation (sporulation septa) and branching, which are characteristics for Actinobacteria (e.g., *Streptomyces*, [43]).

The layers below the crust (layers 4–6) have a crumbly appearance due to the larger size and higher abundance of mineral precipitates and to the less abundance of organic matter between them (Figure 3c,d). When seen under the microscope, the organic matrix of these layers is much less dense than in layers 1–2. It has a porous laminated microstructure with coarser EPS fibers, which are parallel oriented and bundled together, and include many nano- to micro-scale precipitates (Figure 3c,d). Unlike fresher EPS fibers of the upper layers, these older more degraded ones show birefringence under cross-polarized light (Figures 3d and 4b; cf. [40,44–46]). Very few remains of microbes have been observed within this organic matrix, showing only scattered empty and partially degraded sheaths of filamentous microbes. Miliolid foraminifera are also scarcely preserved in these layers. Mineral precipitates of layers 4–6 are also aragonitic and of the same types as those of layers 1–2: (a) subspherical fibrous-radial crystalline particles (Figure 5); and (b) irregular micropeloidal micritic particles (Figures 3d, 4b and 5). However, they are much larger and much more abundant than in layers 1–2. Also, they are typically merged with each other forming complex irregular aggregates of particles, which are larger downwards in the mat, reaching up to 3 cm of width (Figure 4f). In the thin section, these aggregates are composed of individual or coalesced subspherical particles, some of them with a laminated cortex (cf. ‘ooids’ of Suarez-Gonzalez and Reitner. [40]), which are merged together typically by micropeloidal micrite, although crystalline areas are also observed between the merged particles (Figure 5). In layer 4, where the aggregates are smaller and in earlier stages of development, the micritic bridges merging particles together commonly have a meniscus morphology (Figure 5).

3.3. Extractable Lipids within the Studied Mat

In the freely extractable portion, a variety of steroids, hopanoids and fatty acids (FAs) were detected in the studied mat (Figure 14). C₂₇–C₂₉ conventional sterols and distinct C₃₁ sterols were observed in the different mat layers, and low amounts of C₃₀ dinosterols were additionally observed in some of the layers (Table 1a, Figures 15a and 16a). Total sterol concentrations range from 0.65 µg/g dry mat to 32.36 µg/g dry mat, with the highest amounts in the topmost layer 1 (Figure 15a, Table 2). Layer 4a, immediately below the thin mineral crust, shows an enhancement in sterol abundance, being the second highest concentration in the mat. Hopanoids, i.e., hop-22(29)-ene (diploptene), ββ-bishomohopanoic acid, ββ-bishomohopanol, have been observed in all mat layers. The summed hopanoids remarkably increase in layer 4a, up to 70.65 µg/g dry mat (Table S1, Figure 15a). For the FAs (i.e., iso-/anteiso-C₁₅–C₁₇ and unsaturated C_{18:1} and C_{19:1} FAs), their summed concentrations show ranges between 10⁰–10² µg/g dry mat. Like sterols and hopanoids, the abundance of FAs exhibited a significant increase in layer 4a, reaching 230.79 µg/g dry mat (see Tables 2 and S1). In all freely extractable lipids, concentrations in layer 4a were in the same order as in the topmost and biotically active layer 1. Consequently, two declining trends for these three groups of compounds occur in the studied mat: a first one from layer 1 to the thin mineral crust of layer 3, and a second one from layer 4a downwards.

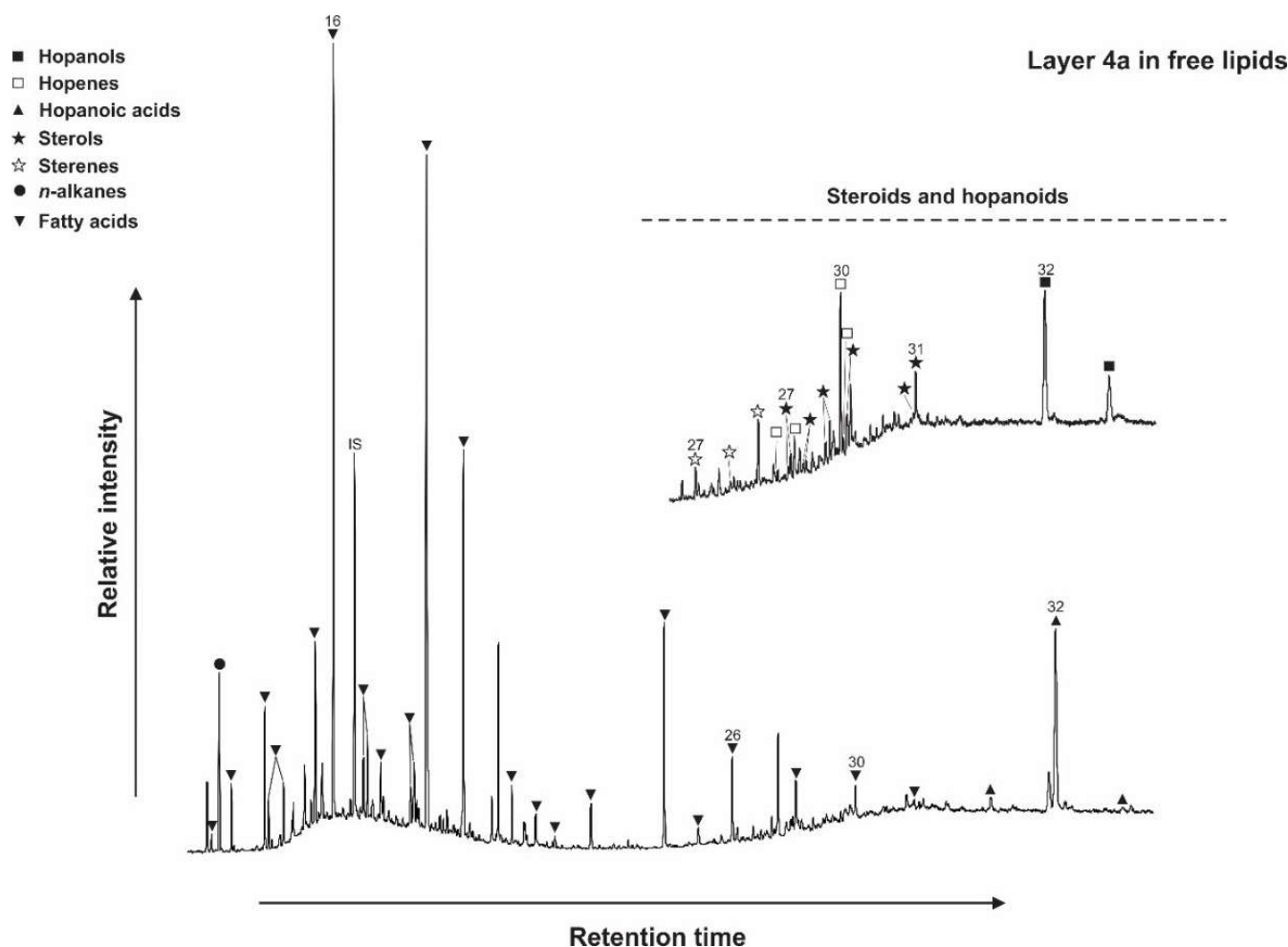


Figure 14. Partial GC-MS chromatograms (total ion current) showing the distribution of freely extractable lipids (TMS derivatives including hopanoids, fatty acids, sterols, and *n*-alkanes) in layer 4a of the microbial mat.

Carbonate-bound lipids also include various sterols, hopanoids and fatty acids as in the freely extractable lipid fraction. For sterols, the summed concentrations are one or two orders of magnitude less abundant than freely extractable sterols, ranging from 0.32 $\mu\text{g/g}$ dry mat to 6.53 $\mu\text{g/g}$ dry mat (Table 1b; Figure 15b). Besides, these carbonate-bound sterols were not detected in the topmost layer 1. Hopanoids in the carbonate-bound fraction were also not detected in layer 1, and in other layers their major summed hopanoids (i.e., hop-17(21)-ene and $\beta\beta$ -bishomohopanoic acid) show lower abundance, an order of magnitude less abundant, than in the freely extractable pool. The highest value is observed in layer 4a (27.87 $\mu\text{g/g}$ dry mat), from which the abundance decreases downwards in the mat (Table 2; Figure 15b). Regarding FAs, similar major groups (i.e., iso-/anteiso- C_{15} - C_{17} and unsaturated $\text{C}_{18:1}$ and $\text{C}_{19:1}$ FAs) were observed, and the summed concentrations are of the same order as in the freely extractable fraction (10^0 – 10^2 $\mu\text{g/g}$ dry mat range). The exception is found in layer 1, where FAs are an order of magnitude less abundant than in the freely extractable lipids (10^2 $\mu\text{g/g}$ dry mat range, see Tables 2 and S2). Interestingly, the summed FAs show a significant increase in abundance in the thin mineral crust (layer 3), and even more enriched in layer 4a (highest concentration: 473.27 $\mu\text{g/g}$ dry mat; Table 2). Below, their abundances decrease sharply, as observed for layer 4b (1.2 $\mu\text{g/g}$ dry mat; Table 2), then similar low abundances are sustained in the deeper mat layers. In both lipid fractions, the relative abundance of C_{31} sterols shows general increase in depth, with a local peak in the thin crust (layer 3), while the other C_{27} – C_{30} sterols decrease downwards in the mat (Figure 16).

Table 1. (a) Concentrations of sterols in the freely extractable lipids of microbial mat layers ($\mu\text{g/g}$ dry mat; n.d. = not detected, modified after Shen et al. [38]). (b) Concentrations of sterols in the carbonate-bound lipids of microbial mat layers ($\mu\text{g/g}$ dry mat; n.d. = not detected, modified after Shen et al. [38]).

| (a) | | | | | | | | | | | | |
|---------------|--|----------------------------|-------------------------------------|---|-------------------------------------|--|--|------------------------------------|---|--|--|---|
| Trivial Names | | Cholesterol | Cholestanol | Brassicasterol | Campesterol | Ergostanol | Stigmasterol | β -Sitosterol | Stigmastanol | Dinosterol | 4 α -Methyl gorgosterol | 4 α -Methyl gorgostanol |
| Compound | | Cholest-5-en-3 β -ol | 5 α -cholestan-3 β -ol | 24-methylcholesta-5,22-dien-3 β -ol | 24-methylcholest-5-en-3 β -ol | 5 α -24-methylcholestan-3 β -ol | 24-ethylcholesta-5,22-dien-3 β -ol | 24-ethylcholest-5-en-3 β -ol | 5 α -24-ethylcholestan-3 β -ol | 4 α ,23,24-trimethylcholest-22-en-3 β -ol | 22,23-methylene-4 α , 23,24-trimethylcholest-5-en-3 β -ol | 22,23-methylene-4 α , 23,24-trimethylcholestan-3 β -ol |
| Layers | | | | | | | | | | | | |
| 1 | | 5.20 | 0.86 | 4.93 | 4.91 | 0.20 | 3.74 | 5.44 | 0.77 | n.d. | 1.10 | 5.21 |
| 2 | | 0.24 | 0.19 | n.d. | 0.34 | 0.06 | 0.43 | 0.77 | 0.19 | n.d. | 0.36 | 1.55 |
| 2b | | 0.89 | 1.96 | 0.52 | 0.54 | 0.99 | 0.89 | 0.94 | 1.85 | 1.05 | 1.07 | 4.71 |
| 3 | | 0.01 | 0.04 | n.d. | 0.02 | 0.02 | 0.02 | 0.03 | 0.05 | n.d. | 0.09 | 0.37 |
| 4a | | 1.15 | 2.01 | 0.51 | 0.52 | 1.19 | 2.03 | 2.78 | 3.37 | 0.82 | 0.39 | 2.72 |
| 4b | | 0.06 | 0.05 | 0.03 | 0.02 | 0.04 | 0.09 | 0.09 | 0.09 | 0.04 | 0.04 | 0.18 |
| 4 | | 0.02 | <0.01 | n.d. | 0.02 | 0.01 | 0.05 | 0.02 | 0.02 | n.d. | 0.12 | 0.40 |
| 5 | | 0.03 | 0.02 | n.d. | 0.07 | 0.04 | 0.16 | 0.12 | 0.13 | n.d. | 0.95 | 2.72 |
| 6 | | 0.08 | <0.01 | n.d. | n.d. | n.d. | 0.08 | 0.02 | 0.01 | n.d. | 0.10 | 0.73 |
| (b) | | | | | | | | | | | | |
| Trivial Names | | Cholesterol | Cholestanol | Brassicasterol | Campesterol | Ergostanol | Stigmasterol | β -Sitosterol | Stigmastanol | Dinosterol | 4 α -Methyl gorgosterol | 4 α -Methyl gorgostanol |
| Compound | | Cholest-5-en-3 β -ol | 5 α -cholestan-3 β -ol | 24-methylcholesta-5,22-dien-3 β -ol | 24-methylcholest-5-en-3 β -ol | 5 α -24-methylcholestan-3 β -ol | 24-ethylcholesta-5,22-dien-3 β -ol | 24-ethylcholest-5-en-3 β -ol | 5 α -24-ethylcholestan-3 β -ol | 4 α ,23,24-trimethylcholest-22-en-3 β -ol | 22,23-methylene-4 α , 23,24-trimethylcholest-5-en-3 β -ol | 22,23-methylene-4 α , 23,24-trimethylcholestan-3 β -ol |
| Layers | | | | | | | | | | | | |
| 1 | | n.d. | n.d. | n.d. | n.d. | n.d. | n.d. | n.d. | n.d. | n.d. | n.d. | n.d. |
| 2 | | 0.02 | <0.01 | n.d. | 0.08 | <0.01 | 0.08 | 0.07 | 0.01 | n.d. | n.d. | 0.34 |
| 2b | | 1.49 | 0.61 | n.d. | n.d. | 0.73 | n.d. | 0.65 | 0.92 | n.d. | n.d. | 2.13 |
| 3 | | 0.04 | 0.05 | n.d. | 0.08 | 0.02 | 0.03 | 0.06 | 0.04 | n.d. | n.d. | 0.40 |
| 4a | | n.d. | 0.36 | n.d. | n.d. | 0.20 | n.d. | n.d. | 0.35 | n.d. | n.d. | n.d. |
| 4b | | 0.09 | 0.05 | n.d. | n.d. | 0.17 | 0.08 | 0.04 | 0.08 | n.d. | 0.04 | 0.18 |
| 4 | | 0.11 | 0.07 | n.d. | 0.12 | 0.03 | 0.25 | 0.12 | 0.09 | n.d. | n.d. | 0.45 |
| 5 | | 0.02 | <0.01 | n.d. | n.d. | n.d. | 0.06 | 0.01 | <0.01 | n.d. | n.d. | 0.22 |
| 6 | | 0.02 | <0.01 | n.d. | 0.03 | <0.01 | 0.04 | 0.03 | 0.01 | n.d. | n.d. | 0.59 |

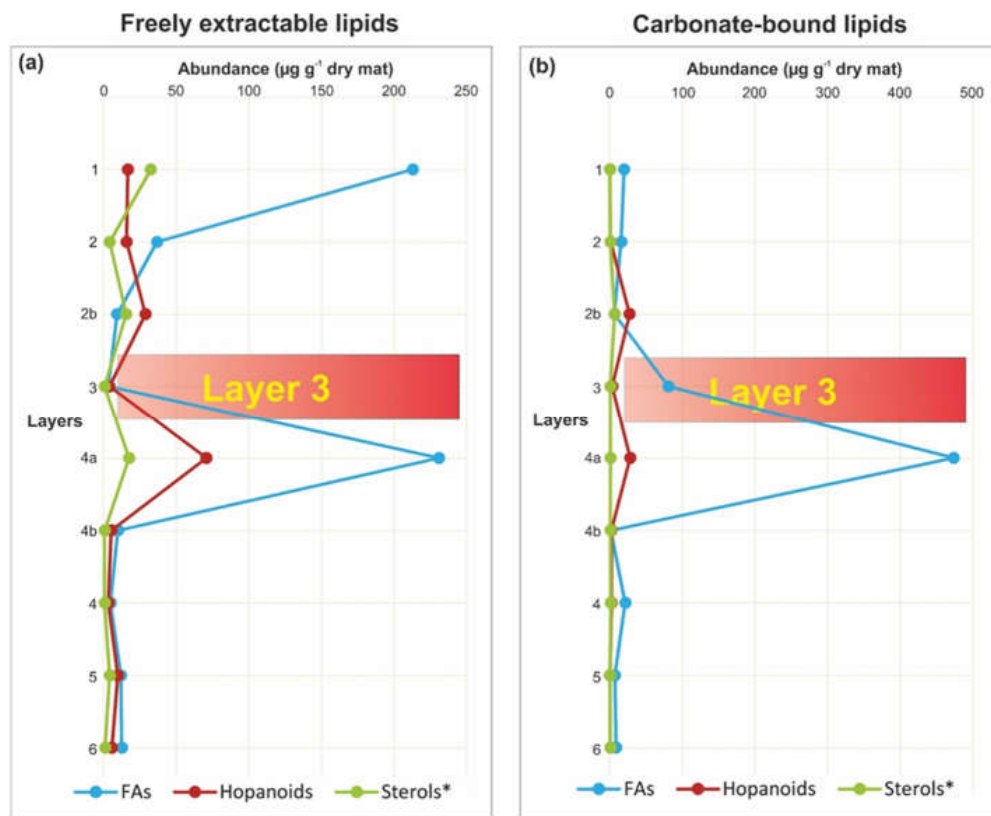


Figure 15. Depth distribution of the summed sterols (carbon ranging C₂₇–C₃₁), hopanoids and fatty acids in the microbial mat layers (µg/g dry mat).

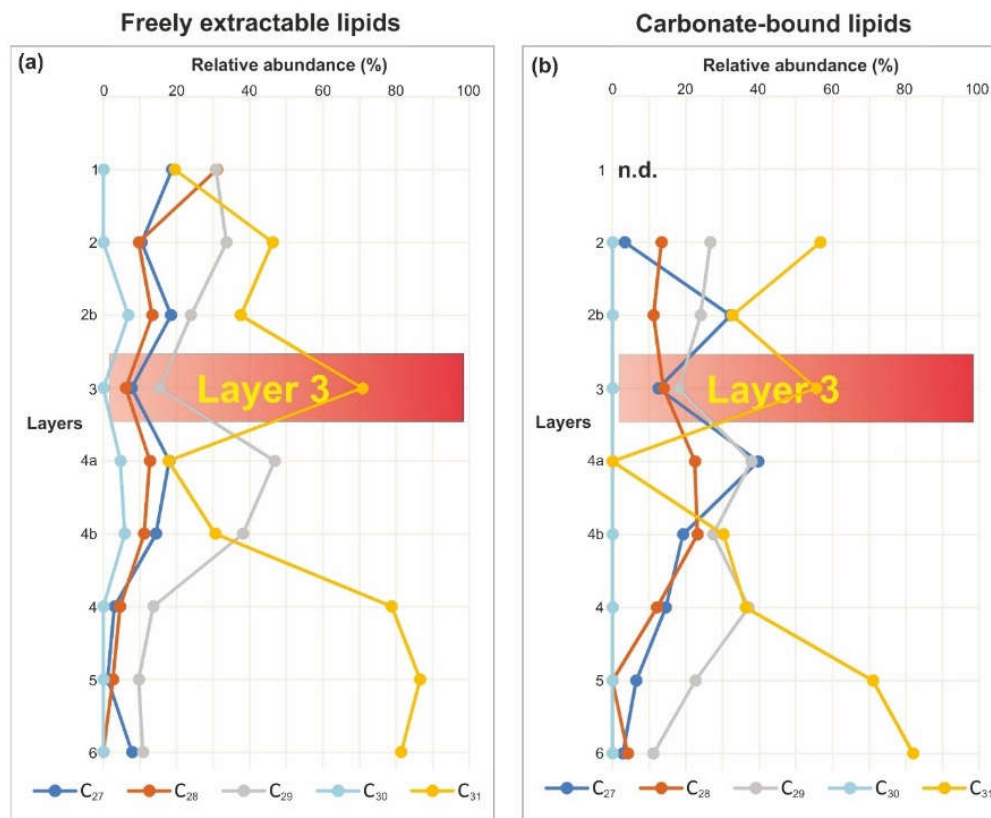


Figure 16. Relative abundance of C₂₇–C₃₁ sterols in the mat profile.

Table 2. Concentrations of summed sterols, major hopanoids and fatty acids (FAs) in freely extractable and carbonate-bound lipids of the microbial mat layers ($\mu\text{g/g}$ dry mat; n.d. = not detected).

| Layer | Freely Extractable Lipids | | | Carbonate-Bound Lipids | | |
|-------|---------------------------|-----------|--------|------------------------|-----------|--------|
| | Sterols * | Hopanoids | FAs | Sterols * | Hopanoids | FAs |
| 1 | 32.36 | 16.67 | 212.72 | n.d. | n.d. | 19.63 |
| 2 | 4.13 | 15.76 | 36.73 | 0.61 | 0.94 | 15.49 |
| 2b | 15.41 | 28.77 | 9.24 | 6.53 | 26.98 | 6.28 |
| 3 | 0.65 | 3.98 | 3.34 | 0.72 | 3.22 | 80.45 |
| 4a | 17.50 | 70.65 | 230.79 | 0.91 | 27.87 | 473.27 |
| 4b | 0.73 | 5.25 | 9.89 | 0.73 | 1.86 | 1.2 |
| 4 | 0.67 | 3.34 | 4.74 | 1.24 | 2.24 | 21.22 |
| 5 | 4.24 | 9.76 | 11.90 | 0.32 | 0.22 | 6.87 |
| 6 | 1.02 | 5.70 | 12.50 | 0.73 | 0.72 | 8.64 |

* Including C₃₀ and C₃₁ sterols.

3.4. Carbon Isotopic Compositions of Microbial Lipids and Hydrocarbons

FAs (including C₁₄-C₂₆ homologues), and hopanoids (including C₃₀ hopene and C₃₂ hopanol) as well as hydrocarbon (C₁₇ *n*-alkane) were identified. GC-C-IRMS measurements revealed relatively high $\delta^{13}\text{C}$ values (i.e., heavier than -20‰) in both lipid fractions of the studied mat, ranging from -15.4 to -20.7‰ for C₁₇ *n*-alkane, -4.4 to -16.4‰ for FAs, -17.6 to -20.2‰ for hopanoids, and -7.2 to -13.3‰ for sterols (Table 3).

Table 3. Carbon isotopic signatures of lipid biomarkers observed in the studied mat (unit: ‰ relative to V-PDB; n.d. = not detected).

| Layer | Compounds | 1 | | 3 | | 5 | | 6 | |
|-------|----------------------------|---------------------------|------------------------|---------------------------|------------------------|---------------------------|------------------------|---------------------------|------------------------|
| | | Freely Extractable Lipids | Carbonate-Bound Lipids |
| | n-alkane | | | | | | | | |
| | 17 | -15.4 | -16.1 | -18.7 | -20.7 | -17.3 | -17.4 | -15.8 | -15.7 |
| | FAs | | | | | | | | |
| | 14:0 | -8.5 | n.d. | n.d. | n.d. | n.d. | n.d. | n.d. | n.d. |
| | iso-15 | n.d. | n.d. | n.d. | -11.8 | n.d. | -16.4 | n.d. | -12.1 |
| | 15:0 | -4.4 | -8.6 | n.d. | -4.7 | n.d. | n.d. | n.d. | -11.0 |
| | 16:1 | -9.4 | -8.7 | n.d. | n.d. | n.d. | n.d. | n.d. | n.d. |
| | iso-16 | n.d. | -9.3 | n.d. | -12.6 | n.d. | -12.4 | n.d. | -12.9 |
| | 16:0 | -6.8 | -12.8 | n.d. | -16.4 | n.d. | -14.3 | n.d. | -13.7 |
| | iso-17 | n.d. | n.d. | n.d. | n.d. | n.d. | -9.3 | n.d. | -12.8 |
| | anteiso-17 | n.d. | n.d. | n.d. | n.d. | n.d. | -10.5 | n.d. | -12.0 |
| | 17:0 | -4.8 | n.d. | n.d. | -12.9 | n.d. | -13.8 | n.d. | -13.3 |
| | 18:1 | -11.6 | -11.4 | n.d. | n.d. | n.d. | n.d. | n.d. | n.d. |
| | 18:0 | n.d. | -11.4 | n.d. | -14.3 | n.d. | -12.5 | n.d. | -12.9 |
| | 19:1 | -11.8 | -10.7 | n.d. | -16.3 | -15.0 | -13.8 | n.d. | -12.9 |
| | 24:0 | n.d. | n.d. | n.d. | -14.8 | -8.5 | -14.4 | -7.8 | -15.1 |
| | 26:0 | n.d. | n.d. | n.d. | -14.5 | n.d. | n.d. | n.d. | -15.9 |
| | Sterols | | | | | | | | |
| | C ₃₁ Δ^0 | -7.2 | n.d. | n.d. | n.d. | -12.5 | n.d. | -13.3 | n.d. |
| | Hopanoids | | | | | | | | |
| | C ₃₀ hopene | n.d. | n.d. | n.d. | n.d. | -20.2 | n.d. | -18.5 | n.d. |
| | C ₃₂ hopanol | n.d. | n.d. | n.d. | n.d. | -17.6 | n.d. | -17.8 | n.d. |

Of all the identifiable isotopic signals, short-chain FAs (including C₁₄-C₁₇) showed highly enriched $\delta^{13}\text{C}$ values (ranging from -4.4 to -14.3‰), while ^{13}C -depletion was observed for their long-chain homologues (including C₁₈-C₂₆; ranging from -10.7 to -16.3‰). $\delta^{13}\text{C}$ values for FAs in the deeper, older layers of the studied mat were consistently depleted by c. 0.2 - 11.5‰ as compared with the top layer 1 (see Table 3). This depletion trend is even stronger in the mineral crust of layer 3, as evident in the long-chain FAs as well as C₁₇ *n*-alkane (see Table 3). Another characteristic feature of carbon isotopic distribution in the

studied mat is that much lighter ^{13}C contents observed for the hopanoids compared with the other lipids (see Table 3), ranging from -17.6 to -20.2% .

4. Discussion

4.1. Interpretation of the Mat Growth History and Significance of the Mineral Crust

The detailed petrographic study of the microbial mat presented here, together with the previously published ^{14}C dates (Figure 1c; Blumenberg et al. [30]) indicate that the mat records two distinct phases of development with dissimilar growth rates, separated by the mineral crust of layer 3 (Figures 1c and 2). The older phase is represented by the three lower layers (4–6, c. 7 cm thick, Figures 1c and 2), which formed in less than 350 years (from 1440 ± 40 to 1111 ± 40 years BP). The younger phase is represented by the two upper layers (1–2, c. 3 cm thick, Figures 1c and 2), which formed in more than 550 years (from 551 ± 40 to 62 ± 40 years BP) and maybe up to 1000 years (if the age of the underlying layer 3, 1111 ± 40 years BP, is considered). Therefore, according to these dates, the younger and thinner phase seems to have accreted at a much slower rate than the older phase.

Despite their different thickness and accretion rate, both mat phases show similar mineral composition, being mainly formed by irregular micritic aggregates with micropeloidal texture and sub-spherical particles with crystalline fibrous-radial texture. These are the typical mineral precipitates of microbial mats from Kiritimati [26,27,40,41], and are also very common in many other examples of modern and fossil microbialites [47–51]. The main difference between the mineral precipitates of the two growth phases is their abundance, size and development stage. In the upper, younger layers, where the EPS matrix is fresher and denser (Figure 3a,b), mineral precipitates are less abundant and developed: irregular micritic particles with micropeloidal texture are few and small, and subspherical fibrous-radial particles are also small and typically not merged with each other (Figures 2 and 4d). On the contrary, in the lower, older layers, where the EPS matrix is scarce and more degraded (Figure 3c,d), subspherical particles are more abundant and merged in large aggregates with micropeloidal micrite between them (Figures 4f and 5). Thus, the taphonomic evolution of EPS downwards in the mat is consistent with the downwards increase in mineral size and abundance, supporting the commonly interpreted role of the degradation of microbial EPS as a trigger to mineral precipitation within microbial communities and to the formation of microbialites [23,44,52,53]. Therefore, the upper and lower parts of the studied sample may be interpreted as two different growth phases of a microbial mat, formed probably under very similar hypersaline environmental conditions. Their difference in accretion rate could have been caused by slight hydrochemical differences, which in turn could have influenced microbial activity and mat accretion. In any case, these two phases represent different development stages: the upper part being the earliest steps of mineralization and the lower part characterizing a more evolved proto-microbialite, after ~ 1400 years of degradation of EPS and of mineral precipitation.

Interestingly, the boundary between those two development stages of the mat is marked by the mineral crust of layer 3, which shows strong contrasts with the other layers (Figures 1c and 2) and with most mineral precipitates previously described from hypersaline mats of Kiritimati [26,27,41]. The ^{14}C dates of the mat (Blumenberg et al. [30]) seem to indicate that the crust was formed during an interruption in microbial mat accretion, c. 1100 years BP. In addition, the strong contrast in mineral precipitation style between the crust and the other mat layers suggests that a significant environmental (i.e., hydrological) change occurred during the interruption in accretion. The μm -scale superposition of fibrous-radial botryoidal laminae (Figure 6c) indicates that precipitation was episodic, yet occurred repeatedly. Similar botryoidal or fan-like fibrous-radial fabrics have been described in fossil microbialites and interpreted to form under different hydrological settings, ranging from freshwater to hypersaline conditions [54,55]. In Kiritimati, the only similar microfabric has been described locally as fibrous aragonite veneers interpreted to precipitate at low CaCO_3 supersaturation [27]. The fact that Kiritimati lakes may experience inflow of fresh groundwater [25] makes it plausible that the interruption in the hypersaline

mat accretion, and the subsequent formation of the crust of layer 3, were related to a hydrochemical change due to freshwater input, which would reduce salinity and alkalinity. A complementary interpretation would be that the environmental change was triggered by a partial or total desiccation of Lake 2. This could be supported by the presence of meniscus precipitates between subspherical particles in layer 4 (the top mat layer of the first development phase), which are typically interpreted as formed in vadose conditions [56–58]. After desiccation, the beginning of the new filling stage of the lake may have had different hydrochemical conditions (e.g., salinity and alkalinity), which could explain the different precipitation mode of the crust. In the context of Lake 2, desiccation episodes are plausible, given the small size of the lake and the strong climatic variability of Kiritimati island, mainly due to ENSO cycles, which strongly influence the water level and salinities of the lakes [24,25,29,40].

Regardless of the exact parameters and conditions that triggered the environmental change between the first hypersaline mat phase (layers 4–6) and the mineral crust of layer 3, that change is further supported by the biotic remains present within the crust (Figures 8–12). Coccoid cyanobacteria are dominant in the current active mat (as in most hypersaline Kiritimati mats [27,28,39], however are only locally preserved within the crust (Figures 6b and 8). Diatom molds are ubiquitous in the crust, although diatoms are absent or very rare in the current hypersaline lake 2 and in the topmost active part of the mat (layer 1), and in addition they are only scarcely preserved in the lower layers 4–6. Similarly, the high abundance of filamentous microbes preserved as molds within the crust contrasts with the currently active mat, dominated by coccoid cyanobacteria. Filamentous cyanobacteria occur in modern hypersaline mats of Kiritimati [27,28], however are morphologically different from the molds observed within the crust, whose size and morphology (Figures 8–12) make them similar to Actinobacteria. Actinobacteria are Gram-positive bacteria with high G+C content and they look like filamentous fungi, forming a mycelium-like network of very thin fibers non-typical for cyanobacteria [43]. The fibers have a thickness of less than a micron and they exhibit various spore-types and sporangia [43]. In addition, the filaments are branching, which is not observed in filamentous cyanobacteria (compare Figure 10b,d with figures in Li et al. [43]). Actinobacteria are common in soil biocrusts [59], which exhibit structural similarities to aquatic stromatolites-microbialites. In Kiritimati, only small amounts of Actinobacteria have been detected within the lower older portions of microbial mats from Lake 21 [28], and they have never been observed in the younger and active parts of hypersaline microbial mats. To our knowledge, there are no previous studies about the possible mineralization behavior of Actinobacteria, and there are very scarce examples of fossilized specimens [60–62]. Therefore, this might be one of the first studies showing their mineralized preservation in carbonate settings. Nevertheless, the fact that their mycelium-like structures are so abundantly and pristinely preserved, not only in the thin crust (layer 3) of the studied microbial mat of Lake 2, however also in similar crusts of older subfossil microbialites from other lakes of Kiritimati (Figure 13), suggests that they have a significant preservation potential in the fossil record, at least under some circumstances, e.g., rapid precipitation of aragonite crusts. The subfossil microbial carbonates of Lakes 21 and 22 are interpreted as the result of a mineralized vein systems, through which shallow groundwater is transported, and which forms a large meter-sized polygonal pattern in the lake [63].

Another interpretation for the filament molds observed within the crust could be that they represent microboring microorganisms (e.g., cyanobacteria, fungi) penetrating the crust botryoids after their precipitation, as occurs in other modern microbial mats and biofilms [64,65]. This interpretation could be supported by the fact that in SEM the filaments are observed to cross through several aragonite crystals (Figure 12). However, the filaments are not observed to penetrate the aragonite botryoids from above and SEM images of the upper surface of the crust do not show circular holes consistent with the size of the filaments. In addition, some of the botryoids are covered by a thin crust of short aragonite crystals, which are not penetrated by these thin filaments (Figures 8a,d and 9a).

Only some of the scarcer brown-colored and larger filaments seem to penetrate the upper part of the crust (Figure 11a), and maybe their lack of fluorescence (Figure 11b) could indicate that they are microborings performed by endoliths that have eliminated, with their perforation, the organic matter present within the crust. In contrast, the highly abundant and smaller filaments do not seem to have been produced by microborers, seeming more like original mat microbes, due to their erected position and tufted grouping, sometimes equivalent to the botryoid shape and size (Figures 8a,d and 9a–c).

Thus, it is interpreted here that both diatoms and Actinobacteria were original microbes of the mat then, and were entombed by a relatively rapid growth of the aragonite botryoids, as observed in other similar fibrous-radial microbial crusts [54]. In fact, some of the aragonite botryoids mimic the shape of filament tufts (Figures 8a,d and 9a–c), indicating that the tufts were probably used as a template for mineral growth. This entombment of original microbes is further supported by the abundant pores of the crust filled by EPS remains (Figure 12b,c,e), suggesting that diatoms and Actinobacteria were part of a microbial community held together by the cohesive action of EPS. Rapid and episodic precipitation of fibrous-radial aragonite botryoidal laminae within the biofilm caused the fossilization of its microbes and EPS within the mineral crust. The contrast in biotic composition of that community with the two phases of hypersaline microbial mat development further suggests that an abrupt modification of environmental parameters (probably a desiccation and/or freshening of the lake) caused the interruption in mat accretion and the subsequent biotic change. In fact, it is noteworthy that Actinobacteria do not occur in modern active microbial mats of the hypersaline lakes of Kiritimati [28,39,66], which contrasts with their extreme abundance within the thin crust of layer 3. The fact that Actinobacteria thrive in special and extreme environments (e.g., Qin et al. [67], and references therein) and that some of them produce antimicrobial substances [68–70] is consistent with a significant environmental change in lake 2, which led to the interruption in accretion of the mat and to a radical modification of its microbial community.

In summary, the evolution of the studied mat is here envisaged as consisting of three stages: (i) a first phase of microbial mat accretion, developed under hypersaline conditions probably very similar to the current ones in Lake 2; (ii) interruption of mat accretion due to an environmental change (probably desiccation and/or freshening of the lake waters), and development of a thin microbial community, which was periodically fossilized by rapid precipitation of fibrous-radial botryoidal aragonite (probably during particular periods of increased alkalinity); (iii) reinstatement of hypersaline conditions in Lake 2, triggering development of a new generation of microbial mat with similar features to phase i. Although equivalent thin fibrous-radial botryoidal crusts have not been previously described in modern mats from Kiritimati, the fact that they occur in several subfossil microbialites (Figure 13), which represent older generations of microbial mats, shows that the formation processes of the crust are relatively common in those environments. In addition, similar fabrics have been described in other microbialite examples [54,55], further pointing to their common occurrence in the geological record.

4.2. Lipid Preservation and Carbonate Precipitation within the Mat

A variety of C₂₇–C₃₁ sterols have been observed in the studied mat, suggesting multiple sources mainly from algae, animals, fungi, and terrestrial plants [38,71–74]. The major portion of GC-amenable hopanoids observed in the mat might be formed as the diagenetic products of bacteriohopanepolys (BHPs; [75–77]) through microbially-driven, progressive defunctionalisation. The predominance of FAs observed are saturated and monounsaturated C₁₆ and C₁₈ together with a cyclopropyl-C₁₉ homologues, implying the primary contributors are bacteria [78–81]. Highly enriched δ¹³C values have been reported for the C₃₁ sterols and the fatty acids from layer 1, indicating their autochthonous input and derived from the CO₂-limited ecosystem of hypersaline Lake 2 [38,82].

Figure 16 shows the relative abundance of the observed sterols in both lipid pools, and the general increase downwards of C₃₁ against C₂₇–C₃₀ sterols (with a particular increase in

the thin crust of layer 3) indicates that C_{31} sterols experienced different degradation patterns compared with the other conventional sterols [38]. Figure 15 shows depth distribution of the summed GC-amenable sterols, hopanoids, and FAs in both lipid fractions. We observe these three group compounds exhibits significant increase in layer 4a, and their summed concentrations of each group are of the same order as the topmost layer 1 (Table 2; Figure 15). In particular, FAs shows very similar abundances between layers 1 and 4a.

These observations support the interpretation that two growth cycles may have occurred in this mat, and that they were interrupted by the formation of the mineral crust of layer 3. Layer 4a, located right below the crust, might represent the once active surface mat community of the first growth phase. Due to the interruption of growth of that first mat (probably due to desiccation and/or freshening of the lake), all microorganisms thriving in the mat and adapted to hypersaline conditions (including the heterotrophic degraders), may have died away relatively fast, at least before its organic matter could be degraded. Subsequently, the surface of that first mat, with its abundant lipids, was sealed by the thin mineral crust, which accreted in relatively fast episodes (as reflected by the pristinely entombed biotic remains). Thus, the mineral crust could isolate the former mat surface and its lipids from further degradation, which would explain the unusual lipid abundance, only comparable to the current surface of the modern hypersaline mat.

In conclusion, it is proposed here that the stable and sustained hypersaline conditions that predominated during both growth phases of the studied mat are very unlikely to produce a significant preservation of biomarkers within the carbonate matrix of the resulting microbialites, as during those periods most lipids would be continuously digested by heterotrophs in the deeper mat layers. Only a special event, such as the drastic environmental change occurred between both growth phases and the subsequent precipitation of the thin mineral crust formed that eliminate the degradation, and rapidly lithify the surface mat community and its organic compounds.

4.3. Relationship between the Mineral Crust and the Carbon Isotope Signature of Lipids

Highly enriched $\delta^{13}C$ values (weighted average c. -10%) were observed for the short-chain FAs in the studied mat, clearly implying their carbon sources were autochthonous and derived from the hypersaline, CO_2 -limited ecosystem of Lake 2 [82]. This ^{13}C -enrichment in microbial lipids is also consistent with high $\delta^{13}C$ values for eukaryotic sterols observed at the top layer 1 of the studied lake 2 mat [38]. Furthermore, the long-chain FAs were generally depleted (by weighted average 0.1–8.2 ‰) than the short-chain homologues, indicating minor contributions from terrestrial higher plants [82]. Hopanoids showed lower $\delta^{13}C$ values than the other lipids, suggesting less amounts of ^{13}C contents that originate from methanogens or anaerobic methane-oxidizing archaea [83]. In addition, van der Meer et al. [84] reported isoprenoid lipids were 7 to 9 ‰ in ^{13}C -depletion relative to the straight-chain lipids, due to the utilization of the reversed tricarboxylic acid cycle. The observed hopanoids results (pentacyclic isoprenoids) in the studied mat are well within the range of the previously published isotope data of isoprenoids [84].

Throughout the mat profile, slightly lighter $\delta^{13}C$ values were observed in the deeper, older growth phase of the mat (layers 5 and 6) than the topmost layer 1, suggesting a decrease in suppression effect caused by CO_2 -limitation of local Lake 2 ecosystem. This is also observed in the mineral crust of layer 3, which shows more ^{13}C -depleted values. Furthermore, FAs and hydrocarbon (i.e., C_{17} *n*-alkane) show stronger ^{13}C -depletions in layer 3, which further supports the interpretation proposed here for the formation of this layer: strong hydrological changes at the end of the first growth cycle of the mat resulting in a significant change of biota, and in the depleted $\delta^{13}C$ value of its lipids, recorded within the thin mineral crust of layer 3.

5. Concluding Remarks

The detailed geomicrobiological work presented here (encompassing different petrographic techniques for both organic and mineral components of the mat, as well as

mineralogical and organic geochemical analyses) shows that the studied microbial mat, from a hypersaline lake of the Kiritimati atoll, had a complex development in its ~1500 years of history. Two main growth phases occurred under hypersaline conditions similar to the current ones. The first growth phase was interrupted by a significant environmental change (probably desiccation and/or freshening of the lake), which led to a modification of the microbiota and to the precipitation of a thin mineral crust. Resumption of the hypersaline conditions produced the second (and actual) growth phase of the mat. During this history, two different types of aragonite precipitation have been recorded. The main growth phases were dominated by the relatively slow formation of subspherical particles and irregular micritic particles with micropeloidal texture, both quite common in microbialites and linked to the degradation of the EPS matrix of the mat. In contrast, the interruption stage between the phases is recorded by a thin and laterally continuous crust composed of superposed fibrous aragonite botryoids, which precipitated in relatively rapid episodes, entombing the microbiota present at the surface.

These two contrasting types of microbially-influenced carbonate precipitation occur within the same microbial mat and they induce very different pathways for the preservation of its lipid biomarkers, both in their abundance and in their carbon isotopes. The lipids present within the thin mineral crust show a particular isotopic signature, different from that of other layers. Furthermore, the relatively rapid precipitation of the crust acted as a seal that protected the lipids immediately below from degradation, causing an abundance and preservation pattern of lipids equivalent to that of a modern active microbial community, despite being >1100 years old. The fact that similar thin, although laterally continuous, crusts occur in subfossil microbialites of Kiritimati and in other microbialite examples indicates that the complex preservation pathways and patterns of biomarkers shown by the studied example have the potential to be more a rule than an exception, and they can be tested in future works on lithifying microbial mats or fossil microbialites. Therefore, this modern example can be used as an analogy for other biomarker investigations, especially since it clearly shows that care must be taken when analyzing microbialite biomarkers: the different microbialite layers and fabrics should be analyzed separately and compared meticulously, and organic geochemistry should always be coupled with thorough petrographic and mineralogical techniques.

Supplementary Materials: The following are available online at <https://www.mdpi.com/article/10.3390/min12020267/s1>, Table S1: Concentrations of major fatty acids (FAs) and hopanoids (hop-17(21)-ene, hop-22(29)-ene, $\beta\beta$ -bishomohopanoic acid, $\beta\beta$ -bishomohopan-32-ol and $\alpha\beta$ -trishomohopan-32-ol) in freely extractable lipids of the microbial mat layers ($\mu\text{g/g}$ dry mat). Table S2: Concentrations of major fatty acids (FAs) and hopanoids (Hop-17(21)-ene, Hop-22(29)-ene, $\beta\beta$ -bishomohopanoic acid, $\beta\beta$ -bishomohopan-32-ol and $\alpha\beta$ -trishomohopan-32-ol) in carbonate-bound lipids of the microbial mat layers ($\mu\text{g/g}$ dry mat).

Author Contributions: Y.S., P.S.-G. and J.R. designed the study. J.R. conducted fieldwork and sampling. Y.S., P.S.-G. and J.R. performed petrographic analyses. Y.S. conducted organic-geochemical analyses. Y.S., P.S.-G. and J.R. discussed and interpreted the data. Y.S. and P.S.-G. wrote the original draft. J.R. participated in the review and editing. All authors have read and agreed to the published version of the manuscript.

Funding: This research has been supported by the German Research Foundation (DFG, Project Re 665/18-2). YS acknowledges funding by the Science and Technology Development Fund, Macau SAR, (FDCT File No. 0002/2019/APD and SKL-LPS (MUST)-2021-2023)) as well as by Ministry of Science and Technology (MOST, Project No. 2021YFA0716100), National Key Research and Development Program, China. PS acknowledges funding by a postdoctoral “Humboldt Research Fellowship” of the Alexander von Humboldt Foundation.

Data Availability Statement: The data presented in this study can be found in the supplement or requested by Yan Shen (yanshen@must.edu.mo).

Acknowledgments: We are very grateful to the editors Vincent V. Barbin and Frédéric Marin as well as the two anonymous reviewers for their valuable comments that helped to improve our manuscript.

We thank Jens Dyckmans for the compound-specific carbon isotope measurements. Volker Thiel and Sebastiaan W. Rampen are acknowledged for their thoughtful and constructive comments. We also thank Wolfgang Dröse, Birgit Röring, and Dorothea Hause-Reitner for the laboratory assistance.

Conflicts of Interest: The authors declare no conflict of interest.

References

1. Scherf, A.-K.; Rullkötter, J. Biogeochemistry of high salinity microbial mats—Part 1: Lipid composition of microbial mats across intertidal flats of Abu Dhabi, United Arab Emirates. *Org. Geochem.* **2009**, *40*, 1018–1028. [[CrossRef](#)]
2. Ley, R.E.; Harris, J.K.; Wilcox, J.; Spear, J.R.; Miller, S.R.; Bebout, B.M.; Maresca, J.A.; Bryant, D.A.; Sogin, M.L.; Pace, N.R. Unexpected diversity and complexity of the Guerrero Negro hypersaline microbial mat. *Appl. Environ. Microbiol.* **2006**, *72*, 3685–3695. [[CrossRef](#)] [[PubMed](#)]
3. Freytet, P.; Plet, A. Modern freshwater microbial carbonates: The Phormidium stromatolites (Tufa-Travertine) of southeastern Burgundy (Paris Basin, France). *Facies* **1996**, *34*, 219–237. [[CrossRef](#)]
4. Bolhuis, H.; Fillinger, L.; Stal, L.J. Coastal Microbial Mat Diversity along a Natural Salinity Gradient. *PLoS ONE* **2013**, *8*, e63166. [[CrossRef](#)] [[PubMed](#)]
5. Ionescu, D.; Spitzer, S.; Reimer, A.; Schneider, D.; Daniel, R.; Reitner, J.; de Beer, D.; Arp, G. Calcium dynamics in microbialite-forming exopolymer-rich mats on the atoll of Kiritimati, Republic of Kiribati, Central Pacific. *Geobiology* **2015**, *13*, 170–180. [[CrossRef](#)]
6. Shiea, J.; Brassel, S.C.; Ward, D.M. Comparative analysis of extractable lipids in hot spring microbial mats and their component photosynthetic bacteria. *Org. Geochem.* **1991**, *17*, 309–319. [[CrossRef](#)]
7. Słowakiewicz, M.; Whitaker, F.; Thomas, L.; Tucker, M.E.; Zheng, Y.; Gedl, P.; Pancost, R.D. Biogeochemistry of intertidal microbial mats from Qatar: New insights from organic matter characterisation. *Org. Geochem.* **2016**, *102*, 14–29. [[CrossRef](#)]
8. Dupraz, C.; Visscher, P.T. Microbial lithification in marine stromatolites and hypersaline mats. *Trends Microbiol.* **2005**, *13*, 429–438. [[CrossRef](#)]
9. van Gemerden, H. Microbial mats: A joint venture. *Mar. Geol.* **1993**, *113*, 3–25. [[CrossRef](#)]
10. Burne, R.V.; Moore, L.S. Microbialites: Organosedimentary Deposits of Benthic Microbial Communities. *PALAIOS* **1987**, *2*, 241. [[CrossRef](#)]
11. Hofmann, H.J.; Grey, K.; Hickman, A.H.; Thorpe, R.I. Origin of 3.45 Ga coniform stromatolites in Warrawoona Group, Western Australia. *Geol. Soc. Am. Bull.* **1999**, *111*, 1256–1262. [[CrossRef](#)]
12. Allwood, A.C.; Walter, M.R.; Kamber, B.S.; Marshall, C.P.; Burch, I.W. Stromatolite reef from the Early Archaean era of Australia. *Nature* **2006**, *441*, 714–718. [[CrossRef](#)] [[PubMed](#)]
13. Thiel, V.; Peckmann, J.; Seifert, R.; Wehrung, P.; Reitner, J.; Michaelis, W. Highly isotopically depleted isoprenoids: Molecular markers for ancient methane venting. *Geochim. Cosmochim. Acta* **1999**, *63*, 3959–3966. [[CrossRef](#)]
14. Benzerara, K.; Menguy, N.; López-García, P.; Yoon, T.-H.; Kazmierczak, J.; Tyliczszak, T.; Guyot, F.; Brown, G.E. Nanoscale detection of organic signatures in carbonate microbialites. *Proc. Natl. Acad. Sci. USA* **2006**, *103*, 9440–9445. [[CrossRef](#)] [[PubMed](#)]
15. Lévillé, R.J.; Fyfe, W.S.; Longstaffe, F.J. Geomicrobiology of carbonate–silicate microbialites from Hawaiian basaltic sea caves. *Chem. Geol.* **2000**, *169*, 339–355. [[CrossRef](#)]
16. Lee, C.; Love, G.D.; Jahnke, L.L.; Kubo, M.D.; Des Marais, D.J. Early diagenetic sequestration of microbial mat lipid biomarkers through covalent binding into insoluble macromolecular organic matter (IMOM) as revealed by sequential chemolysis and catalytic hydrolysis. *Org. Geochem.* **2019**, *132*, 11–22. [[CrossRef](#)]
17. Mißbach, H.; Duda, J.-P.; van den Kerkhof, A.M.; Lüders, V.; Pack, A.; Reitner, J.; Thiel, V. Ingredients for microbial life preserved in 3.5 billion-year-old fluid inclusions. *Nat. Commun.* **2021**, *12*, 1101. [[CrossRef](#)]
18. Tosti, F.; Mastandrea, A.; Guido, A.; Demasi, F.; Russo, F.; Riding, R. Biogeochemical and redox record of mid–late Triassic reef evolution in the Italian Dolomites. *Palaeogeogr. Palaeoclimatol. Palaeoecol.* **2014**, *399*, 52–66. [[CrossRef](#)]
19. Duda, J.-P.; Love, G.D.; Rogov, V.I.; Melnik, D.S.; Blumenberg, M.; Grazhdankin, D.V. Understanding the geobiology of the terminal Ediacaran Khatyspyt Lagerstätte (Arctic Siberia, Russia). *Geobiology* **2020**, *18*, 643–662. [[CrossRef](#)]
20. Duda, J.-P.; Thiel, V.; Bauersachs, T.; Mißbach, H.; Reinhardt, M.; Schäfer, N.; van Kranendonk, M.J.; Reitner, J. Ideas and perspectives: Hydrothermally driven redistribution and sequestration of early Archaean biomass—The “hydrothermal pump hypothesis”. *Biogeosciences* **2018**, *15*, 1535–1548. [[CrossRef](#)]
21. Duda, J.-P.; Blumenberg, M.; Thiel, V.; Simon, K.; Zhu, M.; Reitner, J. Geobiology of a palaeoecosystem with Ediacara-type fossils: The Shibantan Member (Dengying Formation, South China). *Precambrian Res.* **2014**, *255*, 48–62. [[CrossRef](#)]
22. Riding, R. Microbialites, Stromatolites, and Thrombolites. In *Encyclopedia of Geobiology*; Reitner, J., Thiel, V., Eds.; Springer Netherlands: Dordrecht, The Netherlands, 2011; pp. 635–654. ISBN 978-1-4020-9211-4.
23. Dupraz, C.; Reid, R.P.; Braissant, O.; Decho, A.W.; Norman, R.S.; Visscher, P.T. Processes of carbonate precipitation in modern microbial mats. *Earth-Sci. Rev.* **2009**, *96*, 141–162. [[CrossRef](#)]
24. Schoonmaker, J.; Tribble, G.W.; Smith, S.V.; Mackenzie, F.T. Geochemistry of saline ponds, Kiritimati (Republic of Kiribati). *Proc. Fifth Int. Coral Reef Congr.* **1985**, *3*, 439–444.

25. Saenger, C.; Miller, M.; Smittenberg, R.H.; Sachs, J.P. A physico-chemical survey of inland lakes and saline ponds: Christmas Island (Kiritimati) and Washington (Teraina) Islands, Republic of Kiribati. *Saline Syst.* **2006**, *2*, 8. [CrossRef]
26. Trichet, J.; Défarge, C.; Tribble, J.; Tribble, G.; Sansone, F. Christmas Island lagoonal lakes, models for the deposition of carbonate–evaporite–organic laminated sediments. *Sediment. Geol.* **2001**, *140*, 177–189. [CrossRef]
27. Arp, G.; Helms, G.; Karlinska, K.; Schumann, G.; Reimer, A.; Reitner, J.; Trichet, J. Photosynthesis versus Exopolymer Degradation in the Formation of Microbialites on the Atoll of Kiritimati, Republic of Kiribati, Central Pacific. *Geomicrobiol. J.* **2012**, *29*, 29–65. [CrossRef]
28. Schneider, D.; Arp, G.; Reimer, A.; Reitner, J.; Daniel, R. Phylogenetic analysis of a microbialite-forming microbial mat from a hypersaline lake of the Kiritimati atoll, Central Pacific. *PLoS ONE* **2013**, *8*, e66662. [CrossRef]
29. Sachs, J.P.; Sachse, D.; Smittenberg, R.H.; Zhang, Z.; Battisti, D.S.; Golubic, S. Southward movement of the Pacific intertropical convergence zone AD 1400–1850. *Nat. Geosci.* **2009**, *2*, 519–525. [CrossRef]
30. Blumenberg, M.; Thiel, V.; Reitner, J. Organic matter preservation in the carbonate matrix of a recent microbial mat—Is there a ‘mat seal effect’? *Org. Geochem.* **2015**, *87*, 25–34. [CrossRef]
31. Spennemann, D.H.R.; John Head, M. Tongan pottery chronology, 14C dates and the hardwater effect. *Quat. Sci. Rev.* **1998**, *17*, 1047–1056. [CrossRef]
32. Petchey, F.; Clark, G. Tongatapu hardwater: Investigation into the 14C marine reservoir offset in lagoon, reef and open ocean environments of a limestone island. *Quat. Geochronol.* **2011**, *6*, 539–549. [CrossRef]
33. McGregor, H.V.; Hellstrom, J.; Fink, D.; Hua, Q.; Woodroffe, C.D. Rapid U-series dating of young fossil corals by laser ablation MC-ICPMS. *Quat. Geochronol.* **2011**, *6*, 195–206. [CrossRef]
34. Grothe, P.R.; Cobb, K.M.; Bush, S.L.; Cheng, H.; Santos, G.M.; Southon, J.R.; Lawrence Edwards, R.; Deocampo, D.M.; Sayani, H.R. A comparison of U/Th and rapid-screen 14C dates from Line Island fossil corals. *Geochem. Geophys. Geosyst.* **2016**, *17*, 833–845. [CrossRef]
35. Mikutta, R.; Kleber, M.; Kaiser, K.; Jahn, R. Review: Organic matter removal from soils using hydrogen peroxide, sodium hypochlorite, and disodium peroxodisulfate. *Soil Sci. Soc. Am.* **2005**, *69*, 120–135. [CrossRef]
36. Inoue, T.; Illy, E. Feel Like You’re Missing Raman Signal-405 nm Can Help See More. Online Application Note of Hübner Group Company. 2020. Available online: <https://hubner-photonics.com/wp-content/uploads/2020/06/Apps-note-Lasers-for-Raman-using-405-nm-narrow-linewidth.pdf> (accessed on 10 February 2022).
37. Shen, Y.; Thiel, V.; Duda, J.-P.; Reitner, J. Tracing the fate of steroids through a hypersaline microbial mat (Kiritimati, Kiribati/Central Pacific). *Geobiology* **2018**, *16*, 307–318. [CrossRef]
38. Shen, Y.; Thiel, V.; Suarez-Gonzalez, P.; Rampen, S.W.; Reitner, J. Sterol preservation in hypersaline microbial mats. *Biogeosciences* **2020**, *17*, 649–666. [CrossRef]
39. Spring, S.; Brinkmann, N.; Murrja, M.; Spröer, C.; Reitner, J.; Klenk, H.-P. High Diversity of Culturable Prokaryotes in a Lithifying Hypersaline Microbial Mat. *Geomicrobiol. J.* **2015**, *32*, 332–346. [CrossRef]
40. Suarez-Gonzalez, P.; Reitner, J. Ooids forming in situ within microbial mats (Kiritimati atoll, central Pacific). *PalZ* **2021**, *95*, 809–821. [CrossRef]
41. Défarge, C.; Trichet, J.; Jaunet, A.-M.; Robert, M.; Tribble, J.; Sansone, F.J. Texture of microbial sediments revealed by cryo-scanning electron microscopy. *J. Sediment. Res.* **1996**, *66*, 935–947. [CrossRef]
42. Finch, A.A.; Allison, N. Coordination of Sr and Mg in calcite and aragonite. *Mineral. Mag.* **2007**, *71*, 539–552. [CrossRef]
43. Li, Q.; Chen, X.; Jiang, Y.; Jiang, C. Morphological Identification of Actinobacteria. In *Actinobacteria—Basics and Biotechnological Applications*; Dhanasekaran, D., Jiang, Y., Eds.; InTech: London, UK, 2016; ISBN 978-953-51-2248-7.
44. Arp, G.; Hofmann, J.; Reitner, J. Microbial Fabric Formation in Spring Mounds (“Microbialites”) of Alkaline Salt Lakes in the Badain Jaran Sand Sea, PR China. *Palaios* **1998**, *13*, 581–592. [CrossRef]
45. Arp, G.; Reimer, A.; Reitner, J. Calcification in cyanobacterial biofilms of alkaline salt lakes. *Eur. J. Phycol.* **1999**, *34*, 393–403. [CrossRef]
46. Reitner, J.; Peckmann, J.; Blumenberg, M.; Michaelis, W.; Reimer, A.; Thiel, V. Concretionary methane-seep carbonates and associated microbial communities in Black Sea sediments. *Palaeogeogr. Palaeoclimatol. Palaeoecol.* **2005**, *227*, 18–30. [CrossRef]
47. Monty, C.L.V. Chapter 5.1 The Origin and Development of Cryptalgal Fabrics. In *Stromatolites*; Elsevier: Amsterdam, The Netherlands, 1976; pp. 193–249. ISBN 9780444413765.
48. Reitner, J. Modern cryptic microbialite/metazoan facies from Lizard Island (Great Barrier Reef, Australia) formation and concepts. *Facies* **1993**, *29*, 3–40. [CrossRef]
49. Braissant, O.; Cailleau, G.; Dupraz, C.; Verrecchia, E.P. Bacterially Induced Mineralization of Calcium Carbonate in Terrestrial Environments: The Role of Exopolysaccharides and Amino Acids. *J. Sediment. Res.* **2003**, *73*, 485–490. [CrossRef]
50. Dupraz, C.; Reid, R.P.; Visscher, P.T. Microbialites, Modern. *Encycl. Geobiol.* **2011**, 617–635. [CrossRef]
51. Riding, R. The Nature of Stromatolites: 3500 Million Years of History and a Century of Research. In *Advances in Stromatolite Geobiology*; Reitner, J., Quéric, N.-V., Arp, G., Eds.; Springer: Berlin/Heidelberg, Germany, 2011; pp. 29–74. ISBN 978-3-642-10414-5.
52. Reitner, J.; Gautret, P.; Marin, F.; Neuweiler, F. Automicrites in a modern marine microbialites. Formation model via organic matrices (Lizard Island, Great Barrier Reef, Australia). *Bull. Inst. Oceanogr. Monaco-Numero Spec.* **1995**, *14*, 237–303.
53. Arp, G.; Thiel, V.; Reimer, A.; Michaelis, W.; Reitner, J. Biofilm exopolymers control microbialite formation at thermal springs discharging into the alkaline Pyramid Lake, Nevada, USA. *Sediment. Geol.* **1999**, *126*, 159–176. [CrossRef]

54. Camoin, G.; Casanova, J.; Rouchy, J.-M.; Blanc-Valleron, M.-M.; Deconinck, J.-F. Environmental controls on perennial and ephemeral carbonate lakes: The central palaeo-Andean Basin of Bolivia during Late Cretaceous to early Tertiary times. *Sediment. Geol.* **1997**, *113*, 1–26. [[CrossRef](#)]
55. Kirkham, A.; Tucker, M.E. Thrombolites, spherulites and fibrous crusts (Holkerian, Purbeckian, Aptian): Context, fabrics and origins. *Sediment. Geol.* **2018**, *374*, 69–84. [[CrossRef](#)]
56. Flügel, E.; Munnecke, A. *Microfacies of Carbonate Rocks: Analysis, Interpretation and Application*, 2nd ed.; Springer: Berlin/Heidelberg, Germany, 2010; ISBN 9783642037955.
57. Tucker, M.E.; Wright, V.P. *Carbonate Sedimentology*; Blackwell Scientific Publications: Oxford, UK, 1990.
58. Dunham, R.J. Meniscus cement. In *Carbonate Cements*; Bricker, O.P., Ed.; Johns Hopkins Univ Stud Geol: Baltimore, MD, USA, 1971.
59. Omari, H.; Pietrasiak, N.; Ferrenberg, S.; Nishiguchi, M.K. A spatiotemporal framework reveals contrasting factors shape biocrust microbial and microfaunal communities in the Chihuahuan Desert. *Geoderma* **2022**, *405*, 115409. [[CrossRef](#)]
60. Wilkinson, H.P. Fossil actinomycete filaments and fungal hyphae in dicotyledonous wood from the Eocene London Clay, Isle-of-Sheppey, Kent, England. *Bot. J. Linn. Soc.* **2003**, *142*, 383–394. [[CrossRef](#)]
61. Waggoner, B.M. Fossil actinomycete in Eocene-Oligocene Dominican amber. *J. Paleontol.* **1994**, *68*, 398–401. [[CrossRef](#)]
62. Girard, V.; Adl, S.M. Amber microfossils: On the validity of species concept. *Comptes Rendus Palevol* **2011**, *10*, 189–200. [[CrossRef](#)]
63. Reitner, J. Das Salz der Erde “Leben im Extremen”. Gaia Inform 2011. Geowissenschaftliches Museum: Göttingen, Germany, 2011.
64. Perry, C.T. Biofilm-related calcification, sediment trapping and constructive micrite envelopes: A criterion for the recognition of ancient grass-bed environments? *Sedimentology* **1999**, *46*, 33–45. [[CrossRef](#)]
65. Reid, R.P.; Foster, J.S.; Radtke, G.; Golubic, S. Modern Marine Stromatolites of Little Darby Island, Exuma Archipelago, Bahamas: Environmental Setting, Accretion Mechanisms and Role of Euendoliths. In *Advances in Stromatolite Geobiology*; Reitner, J., Quéric, N.-V., Arp, G., Eds.; Springer: Berlin/Heidelberg, Germany, 2011; pp. 77–89, ISBN 978-3-642-10414-5.
66. Schmitt, S.; Conroy, J.L.; Flynn, T.M.; Sanford, R.A.; Higley, M.C.; Chen, M.; Fouke, B.W. Salinity, microbe and carbonate mineral relationships in brackish and hypersaline lake sediments: A case study from the tropical Pacific coral atoll of Kiritimati. *Depos. Rec* **2019**, *5*, 212–229. [[CrossRef](#)]
67. Qin, S.; Li, W.-J.; Dastager, S.G.; Hozzein, W.N. Editorial: Actinobacteria in Special and Extreme Habitats: Diversity, Function Roles, and Environmental Adaptations. *Front. Microbiol.* **2016**, *7*, 1415. [[CrossRef](#)]
68. Mahajan, G.B.; Balachandran, L. Antibacterial agents from actinomycetes—a review. *Front Biosci.* **2012**, *4*, 240–253. [[CrossRef](#)]
69. Verma, E.; Chakraborty, S.; Tiwari, B.; Mishra, A.K. Antimicrobial Compounds from Actinobacteria. In *New and Future Developments in Microbial Biotechnology and Bioengineering*; Elsevier: Amsterdam, The Netherlands, 2018; pp. 277–295, ISBN 9780444639943.
70. Musa, Z.; Ma, J.; Egamberdieva, D.; Abdelshafy Mohamad, O.A.; Abaydulla, G.; Liu, Y.; Li, W.-J.; Li, L. Diversity and Antimicrobial Potential of Cultivable Endophytic Actinobacteria Associated With the Medicinal Plant *Thymus roseus*. *Front. Microbiol.* **2020**, *11*, 191. [[CrossRef](#)]
71. Atwood, A.R.; Volkman, J.K.; Sachs, J.P. Characterization of unusual sterols and long chain diols, triols, keto-ols and n-alkenols in El Junco Lake, Galápagos. *Org. Geochem.* **2014**, *66*, 80–89. [[CrossRef](#)]
72. Houle, H.M.; Lopez, C.B.; Leblond, J.D. Sterols of the Toxic Marine Dinoflagellate, *Pyrodinium bahamense*. *J. Eukaryot. Microbiol.* **2019**, *66*, 528–532. [[CrossRef](#)] [[PubMed](#)]
73. Volkman, J.K. A review of sterol markers for marine and terrigenous organic matter. *Org. Geochem.* **1986**, *9*, 83–99. [[CrossRef](#)]
74. Volkman, J.K. Sterols and other triterpenoids: Source specificity and evolution of biosynthetic pathways. *Org. Geochem.* **2005**, *36*, 139–159. [[CrossRef](#)]
75. Rohmer, M.; Bouvier-Nave, P.; Ourisson, G. Distribution of hopanoid in prokaryotes. *J. Gen. Microbiol.* **1984**, *130*, 1137–1150.
76. Blumenberg, M.; Berndmeyer, C.; Moros, M.; Muschalla, M.; Schmale, O.; Thiel, V. Bacteriohopanepolyols record stratification, nitrogen fixation and other biogeochemical perturbations in Holocene sediments of the central Baltic Sea. *Biogeosciences* **2013**, *10*, 2725–2735. [[CrossRef](#)]
77. Johnson, S.S.; Graham, H.V.; Des Marais, D.J.; Hazen, R.M.; Meadows, V.; Arney, G.N.; Schmidt, B.E. Detecting life on Earth and the limits of analogy. *Planet. Astrobiol.* **2020**, *1*, 121–150.
78. Kaneda, T. Iso- and anteiso-fatty acids in bacteria: Biosynthesis, function, and taxonomic significance. *Microbiol. Rev.* **1991**, *55*, 288–302. [[CrossRef](#)]
79. Taylor, J.; Parkes, J. Identifying different populations of sulphate-reducing bacteria within marine sediment systems, using fatty acid biomarkers. *J. Gen. Microbiol.* **1985**, *131*, 631–642. [[CrossRef](#)]
80. Teece, M.A.; Fogel, M.L.; Dollhopf, M.E.; Nealson, K.H. Isotopic fractionation associated with biosynthesis of fatty acids by a marine bacterium under oxic and anoxic conditions. *Org. Geochem.* **1999**, *30*, 1571–1579. [[CrossRef](#)]
81. de Kluijver, A.; Nierop, K.G.J.; Morganti, T.M.; Bart, M.C.; Slaby, B.M.; Hanz, U.; de Goeij, J.M.; Mienis, F.; Middelburg, J.J. Bacterial precursors and unsaturated long-chain fatty acids are biomarkers of North-Atlantic deep-sea demosponges. *PLoS ONE* **2021**, *16*, e0241095. [[CrossRef](#)]
82. Schouten, S.; Hartgers, W.A.; López, J.F.; Grimalt, J.O.; Sinninghe Damsté, J.S. A molecular isotopic study of ¹³C-enriched organic matter in evaporitic deposits: Recognition of CO₂-limited ecosystems. *Org. Geochem.* **2001**, *32*, 277–286. [[CrossRef](#)]

-
83. Pancost, R.D.; Pagani, M. Controls on the Carbon Isotopic Compositions of Lipids in Marine Environments. In *Marine Organic Matter: Biomarkers, Isotopes and DNA*; Volkman, J.K., Ed.; Springer: Berlin/Heidelberg, Germany, 2006; pp. 209–249, ISBN 3-540-28401-X.
 84. van der Meer, M.T.J.; Schouten, S.; Sinninghe Damsté, J.S. The effect of the reversed tricarboxylic acid cycle on the ^{13}C contents of bacterial lipids. *Org. Geochem.* **1998**, *28*, 527–533. [[CrossRef](#)]